Supplementary Information

Interfacial hydride transfer for dehalogenation with water

Li Gong[1,2#], Shuge Wang[1#], Furong Guo[2#], Zekun Zhao[1], Yingying Ma[1], Yuqing Zhang[1], Qian Zheng[2], Meiqi Li[2*], Lizhi Zhang[2]

[1]College of Environment, Zhejiang University of Technology, Hangzhou 310014, P. R. China

[2]State Key Laboratory of Green Papermaking and Resource Recycling, School of Environmental Science and Engineering, Shanghai Jiao Tong University, Shanghai 200240, P. R. China

* Correspondence to: maggielmq@sjtu.edu.cn.

[#] These authors contributed equally to this work.

Summary

Number of pages: 71

Number of texts: 10

Number of figures: 37

Number of tables: 13

Table of Contents

89

Supplementary Texts

Text 1:

Chemicals. Sodium metasilicate (Na_2SiO_3, 44-47%), Reduced iron powder and deuterium oxide (D_2O) were purchased from Aladdin (Shanghai, China). Florfenicol ($C_{12}H_{14}Cl_2FNO_4S$, 99.5%) was supplied by Meclin (Shanghai, China). Deschloro florfenicol (dFF, $C_{12}H_{15}ClFNO_4S$, 95%) and dideschloro Florfenicol (ddFF, $C_{12}H_{16}FNO_4S$, 95%) were provided by Achem-Block. 1,3-dimethyl-2-phenyl-1H-benzo[*d*]imidazol-3-ium (BIM^+, 95%) was procured from Hangzhou Bangyi Chemical Corporation. Reduced iron powder was stored under an argon atmosphere before use.

Methanol, n-hexane, sodium hydroxide (NaOH), sodium borohydride ($NaBH_4$), hydrochloric acid (HCl), and HEPES (4-(2-hydroxyethyl)-1-piperazineethanesulfonic acid), along with liquid chlorinated compounds, including trichloroethylene (TCE), perchloroethylene(PCE), chloroform (CF), *cis*-1,2-dichloroethene (*cis*-DCE), *trans*-1,2-dichloroethene (*trans*-DCE), and vinyl chloride (VC), were sourced from Aladdin (Shanghai, China). Trichloroacetic acid (TCAA) and deuterated acetic acid (AA-d_4) were all obtained from Shanghai Titan Scientific Co., Ltd. Gaseous standards, including methane, ethane, acetylene, propene, propane, butylene, butane, pentene, pentane, hexene, and hexane, were provided by Dalian Special Gases Co., Ltd. Ultra-high purity nitrogen, hydrogen, and air for gas chromatography were supplied by Hangzhou Special Gases Co., Ltd.

All solutions were prepared with deionized water that had been deoxygenated by bubbling nitrogen for 60 min at room temperature.

Text 2:

Preparation of $SiH^{\delta-}$-ZVI and Si-ZVI. To synthesize $SiH^{\delta-}$-ZVI, 2.44 g of ZVI powder, 0.053 g of sodium silicate, and 69 μL of deionized water (used as a grinding aid) were homogeneously mixed and then subjected to ball milling in a 100 mL grinding jar containing 50 zirconia beads (6 mm in diameter). The ball milling was conducted at 400 rpm for 20 hours under an argon atmosphere at room temperature. Detailed procedures of the mechanochemical process can be found in our previous publications.[1-5] As a control, Si-doped ZVI (Si-ZVI) was prepared using the same method as $SiH^{\delta-}$-ZVI but without the addition of the grinding aid. Additionally, $SiD^{\delta-}$-ZVI was synthesized by replacing deionized water with D_2O under identical ball milling conditions, denoted as $SiD^{\delta-}$-ZVI. After the ball milling process was completed, the samples were collected in a nitrogen-filled glove bag and subsequently stored in an argon-filled glove box for further use.

Text 3:

Material Characterizations. The crystalline phases of the ZVIs were characterized by X-ray diffraction (XRD; Rigaku D/max-2200PC, Japan) using Cu Kα radiation (λ = 1.54056 Å) over a 2θ range of 20-80°. Data were analyzed by Rietveld refinement using MDI Jade 6.5 software and the ICSD database. Surface composition was analyzed by X-ray photoelectron spectroscopy (XPS; Thermo Scientific K-Alpha) and Fourier-transform infrared spectroscopy (FTIR; Thermo Scientific Nicolet iS20). XPS data were calibrated against the C 1*s* peak at 284.8 eV and were analyzed by XPSpeak 4.1 software. FTIR spectra were analyzed using Thermo OMNIC 9.2 software.

Time-of-Flight Secondary Ion Mass Spectrometry (TOF-SIMS, IONTOF TOF.SIMS 5, Germany) was used to analyze the formation of chemical bonds on the materials. Powder samples were evenly spread on copper conductive adhesive, and a Bi_3^+ ion beam was employed to bombard the samples for collecting mass spectral data, which enabled the characterization of surface chemical bonding states.

Particle morphology and elemental distribution were assessed through high-angle annular dark-field scanning transmission electron microscopy (HAADF-STEM; FEI Talos F200X) equipped with energy-dispersive spectroscopy (EDS; FEI Super X, USA). The operational settings for the microscope included an acceleration voltage of 200 kV, power of 5 kW, and current of 202 μA. High-resolution transmission electron microscopy (HRTEM) images were acquired using an FEI Tecnai G2 F20. For sample preparation, ZVI powder was diluted in ethanol and sonicated for 30 minutes to ensure homogeneity, followed by deposition of a drop of the suspension onto a holey carbon-coated 300 mesh Cu TEM grid, which was then dried at room temperature. Lattice fringes extracted from HRTEM micrographs were further analyzed using DigitalMicrograph 3.2 software.

The specific surface area was determined through Brunauer–Emmett–Teller (BET) nitrogen adsorption at 100 K utilizing an ASAP2460 instrument (Micromeritics, USA).

The Fe^0 content of the prepared ZVI particles was quantified via acid digestion. Briefly, around 10 mg of ZVI sample was dispersed in a mixed solution containing 1 mL of 37% concentrated HCl and 4 mL of deoxygenated ultrapure water, following a previously reported protocol.[6] The mixture was shaken continuously for 12 h to ensure sufficient reaction. The produced hydrogen gas was subsequently analyzed using a GC-TCD system (Agilent 9790

GC). The final Fe^0 content was calculated based on the stoichiometric relationship defined in **Eq. S1**.

$$Fe^0 + 2H^+ \rightarrow Fe^{2+} + H_2\uparrow \quad (S1)$$

Electrochemical properties. Electrochemical analysis, including Tafel curves, Electrochemical impedance spectroscopy (EIS), were performed using a CHI-760e Electrochemical Workstation (CHI Instruments, Chenhua, China, Shanghai) in a standard three-electrode system according previous studies.[4,5,7] A glassy carbon electrode was used as the working electrode, coated with a 0.4 mm thick iron powder layer, with an effective area of 1 mm^2.[8] Ag/AgCl served as the reference electrode, and a platinum (Pt) counter electrode. The electrolyte was 0.1 M sodium sulfate (Na_2SO_4). After recording the open circuit potential (OCP) for 1 hour, EIS measurements were performed at the OCP with a sinusoidal potential perturbation amplitude of 5 mV, over a frequency range of 100 kHz to 10 mHz.[9,10] Finally, Tafel curve tests were carried out at a scan rate of 0.01 V/s, with a potential range of -1.2 V to -0.5 V. EIS data were fitted and analyzed via ZSimpWin 3.6 software.

Text 4: Batch experiments of FF degradation.

FF Degradation by ZVI, Si-ZVI, $SiH^{\delta-}$-ZVI and $SiD^{\delta-}$-ZVI. The degradation experiments of 20 ppm florfenicol (FF) were conducted by adding 0.40 g of ZVIs to 40 mL of deoxygenated HEPES buffer solution (pH 7) in 64 mL anaerobic glass bottles. The bottles were sealed with PTFE-lined caps and placed in a shaking incubator at 25 °C, operating at 30 rpm, to maintain anaerobic conditions throughout the experiment. Samples were collected at the

specified time and filtered through a 0.22 μm membrane to remove the nanohybrid for subsequent degradation product analysis.

Analysis of Degradation Products. Concentrations of FF, dFF, and ddFF in filtered aqueous samples were determined using a High-Performance Liquid Chromatography (HPLC) system (Agilent 1260 Infinity II) equipped with a UV detector set at 224 nm, according to previous studies. Chromatographic separation was achieved using an Eclipse Plus C18 column (4.6 × 100 mm) with a mobile phase consisting of methanol/water (45:55, v/v) at a flow rate of 0.8 mL/min. The injection volume for each sample was 10 μL.

Systematic identification of FF degradation products was performed using Ultra-Performance Liquid Chromatography coupled with Quadrupole Time-of-Flight Tandem Mass Spectrometry (UPLC-Q-TOF MS/MS, Agilent 1290-6545 system).[4,11] Chromatographic separation was performed on an Eclipse Plus C18 column (4.6 mm × 100 mm) with a 3 μL injection volume. A gradient elution program was employed, using 5 mM ammonium acetate in water and methanol as mobile phases at a flow rate of 0.3 mL/min. The program initiated at 50% methanol, ramped to 100% methanol over 1 min, held for 3 min, returned to 50% methanol at 3.1 min, and re-equilibrated for 5 min. Mass spectrometric detection utilized electrospray ionization in negative mode with the source temperature at 300 °C and ionization voltage at 2000 V. Nitrogen served as the curtain (10 Arb) and auxiliary gas (12.5 Arb). Data were acquired in enhanced MS mode across a mass range of 50-500 *m/z*. The acquired UPLC-Q-TOF MS/MS data were analyzed using Agilent Qualitative Analysis B.07.00 software.

Analysis of Dehalogenation. The concentrations of chloride (Cl^-) and fluoride (F^-) ions released after FF degradation for 40 days by $SiH^{\delta-}$-ZVI and Si-ZVI were measured by ion

chromatography (ICS-1100). Prior to analysis, supernatant samples were filtered and sequentially passed through Na-type and reversed-phase solid-phase extraction cartridges to eliminate interfering metal ions and organic macromolecules.

Analysis of Silicon Leaching. To evaluate the chemical stability of the silicate shell, the concentration of dissolved silicon in the reaction solution was measured at 1, 3, 7, 10, and 20 d. At each time point, an aqueous sample was collected, filtered through a 0.22 μm PES membrane, and the filtrate was digested with nitric acid at 250 °C for 1 h. After cooling, the solution was diluted to 10 mL with ultrapure water and analyzed by ICP-MS (Agilent 7900 ICP-MS) under optimized conditions (RF power = 1550 W, carrier Ar flow = 1.05 $L \cdot min^{-1}$, auxiliary gas flow = 0.9 $L \cdot min^{-1}$, sampling depth = 8 mm).[12] Silicon concentrations were quantified using calibration curves from standard solutions (0-1000 $\mu g \cdot L^{-1}$). The cumulative silicon leaching ratio was calculated based on the total silicon content in the as-prepared $SiH^{\delta-}$-ZVI.

Influence of BIM^+ on FF degradation by Si-ZVI and $SiH^{\delta-}$-ZVI. To further clarify the mechanistic role of surface $Si–H^{\delta-}$ in the reductive dehalogenation process in the $SiH^{\delta-}$-ZVI system, quenching experiments were performed. BIM^+ was used as a quencher for surface $Si–H^{\delta-}$ and added to the reaction system to obtain a predetermined BIM^+ concentration (0.4 mM).[13] HEPES buffer solution was then added to establish the reaction, followed by the addition of $SiH^{\delta-}$-ZVI or Si-ZVI to initiate the reaction. Except for the addition of the quencher, all other experimental procedures and reaction conditions were the same as those used in the FF batch experiments.

EPR Analysis of FF degradation by Si-ZVI and $SiH^{\delta-}$-ZVI. To identify the carbon-

centered radical intermediate formed during the dechlorination of FF by Si-ZVI and $SiH^{\delta-}$-ZVI, electron paramagnetic resonance (EPR) spectroscopy was performed using 5,5-dimethyl-1-pyrroline N-oxide (DMPO) as the spin-trapping agent.[14] Specifically, 1 $g \cdot L^{-1}$ of $SiH^{\delta-}$-ZVI and Si-ZVI was added to 10 mL of anoxic water (20 mL sealed vial) containing predetermined concentrations of FF, DMPO. Vials were rotated (30 rpm) at 25 ± 2 °C, with time-resolved samples collected and analyzed by EPR immediately. EPR spectra were acquired on a Bruker EMXplus-6/1 spectrometer (variable-temperature control; copper-constantan thermocouple monitoring) with settings: microwave power = 6.325 mW, modulation amplitude = 0.05 mT, modulation frequency = 100 kHz, scan time = 30 s.

To further identify the structure of the spin-trapping adducts formed during the above EPR experiments, the reaction mixtures were analyzed by Ultra-Performance Liquid Chromatography-Tandem Mass Spectrometry (UPLC-Q-TOF MS/MS).[15] Aliquots were withdrawn from sealed vials at designated time points, immediately filtered through a 0.22 μm membrane, and the resulting supernatants were directly injected for analysis. The analytical conditions were identical to those used for degradation product analysis.

***In-situ* FTIR analysis of FF degradation.** The reaction process of FF degradation by $SiH^{\delta-}$-ZVI was monitored by *In-situ* FTIR spectroscopy. *In-situ* FTIR spectra were collected at different time intervals to track the changes in functional groups during the reaction, thereby elucidating the degradation mechanism and intermediate products. Spectral acquisition was performed with a resolution of 4 cm^{-1} over the range of 600–4000 cm^{-1}, and background spectra were collected beforehand for calibration. All collected FTIR spectra were analyzed using Thermo OMNIC software.

Text 5: Analysis of Si–H$^{\delta-}$ regeneration.

***In-situ* Raman Spectroscopy.** The regeneration of Si–H$^{\delta-}$ on SiH$^{\delta-}$-ZVI after FF degradation was monitored by *in situ* Raman spectroscopy (LabRAM HR Evolution, Horiba, France).[16,17] SiH$^{\delta-}$-ZVI (0.4 g) was reacted with 20 ppm FF in H_2O or D_2O for 1 h. The reacted materials were then immersed in the corresponding solvent (H_2O or D_2O). Spectra were acquired at 0, 10, 20, 30, 40, 50, and 60 min over the range of 400–4000 cm^{-1}, using a 532 nm excitation laser with an acquisition time of 120 s, to track the evolution of Si–H$^{\delta-}$/Si–D$^{\delta-}$ Si–OH$^{\delta+}$/Si–OD$^{\delta+}$, and the O–H stretching band. All collected Raman spectra were analyzed using Origin 2021 software.

***In-situ* FTIR Spectroscopy.** *In situ* Fourier transform infrared (FTIR) spectroscopy (Nicolet iS50, Thermo Fisher Scientific, USA) was performed to further probe the regeneration of Si–H$^{\delta-}$. Sample preparation and reaction conditions were identical to those for *in-situ* Raman analysis. FTIR spectra were recorded over 400–4000 cm^{-1} at the same time intervals to monitor changes in Si–H$^{\delta-}$/Si–D$^{\delta-}$, Si–OH$^{\delta+}$/Si–OD$^{\delta+}$ and the O–H stretching band. All collected FTIR spectra were analyzed using Thermo OMNIC software.

CV analysis. Cyclic voltammetry (CV) measurements were performed using a CHI-760e Electrochemical Workstation (CHI Instruments, Chenhua, China, Shanghai) in a standard three-electrode system.[7,18] A glassy carbon electrode was used as the working electrode, coated with a 0.4 mm thick iron powder layer, with an effective area of 1 mm^2. Ag/AgCl was used as the reference electrode, and a platinum (Pt) electrode as the counter electrode. The electrolyte was 0.1 M sodium sulfate (Na_2SO_4). CV measurements were conducted by scanning from different initial potentials (-0.8 to -1.05 V vs. Ag/AgCl) to a fixed upper potential of 0.4 V.[19,20]

All potentials were converted from the Ag/AgCl reference electrode to the reversible hydrogen electrode (RHE) scale using the following equation:

$$E_{RHE} = E_{Ag/Cl} + 0.0591 * pH + 0.1976\ V \quad (S2)$$

where 0.1976 V corresponds to the standard potential of the Ag/AgCl electrode (saturated KCl) at 25 °C. All potentials in this work are reported in volts (V).

Text 6: Batch experiments of chlorinated hydrocarbon dechlorination.

In the experiment on chlorinated hydrocarbon (CHC) degradation, 0.26 g of $SiH^{\delta-}$-ZVI was added to a 52 mL glass bottle, following experimental conditions consistent with those previously employed for ZVI-mediated reductive dechlorination.[1-3,5,7] Chlorinated hydrocarbons including TCE, CF, *cis*-DCE, *trans*-DCE, VC, and PCE were dissolved in methanol. This diluted solution was introduced into the reaction system to achieve a contaminant concentration of 100 μM. All bottles containing the solution were sealed with PTFE caps and placed in a temperature-controlled incubator rotating at 30 rpm, with the temperature maintained at room temperature (25 ± 2 °C).

At predetermined time intervals, gaseous products were analyzed using an Agilent 7890B Gas Chromatograph (GC) equipped with a GS-Q column (0.53 mm × 30 m, Agilent Technologies). The oven temperature was initially set at 50 °C and held for 7 minutes, then increased at a rate of 20 °C/min to 230 °C, where it was held for approximately 10 minutes. This temperature program achieved complete separation of alkanes, chlorinated compounds, and unreacted chlorinated hydrocarbons. These experimental conditions were designed to ensure accurate detection and analysis of the target products, thereby providing reliable data for the study.

Text 7: Calculations of electron efficiency.

The generic half-reaction of CHC reductive dechlorination can be written as in **Eq. S3**. Several dechlorination products (*e.g.*, methane, ethylene and ethane, etc.) are possible during its dechlorination by ZVIs, which have different values of n, m, and g (**Eq. S3**). By quantifying all products, the quantity of electrons utilized for TCE reduction (N_e) can be calculated using **Eq. S4**.[6] The value of N_t (the total quantity of electrons provided by ZVI) equal the sum of the electrons used for reducing target contaminant (to all products) and those for reducing H_2O (**Eq. S5)**.[21] Consequently, the ε_e for CHC dechlorination can be defined as **Eq. S6**, as described in previous studies.[3,5,21-25]:

$$\text{chlorinated ethene} + n\cdot e^- + m\cdot H^+ \rightarrow \text{products} + g\cdot Cl^- \quad \text{(S3)}$$

$$N_e = \sum_i n_i p_i \quad \text{(S4)}$$

$$N_t = \sum_i n_i p_i + 2M_{H_2} \quad \text{(S5)}$$

$$\varepsilon_e = \frac{\sum_i n_i p_i}{\sum_i n_i p_i + 2M_{H_2}} \quad \text{(S6)}$$

where n_i is the stoichiometry of product i from the reduction of the target contaminant and p_i is the molar quantity of that product. M_{H_2} is the molar quantity of H_2 produced during the FF dechlorination. Note that each mol of H_2 formed from H^+/H_2O requires 2 moles of electrons ($H^+ + 2e \rightarrow H_2(g)$).

Text 8: Practical applications of $SiH^{\delta-}$-ZVI for groundwater remediation.

Batch Experiment of TCE dechlorination in Real groundwater. In addition to HEPES buffer, TCE hydrodechlorination by $SiH^{\delta-}$-ZVI and ZVI was also evaluated using real groundwater collected from an industrial site in Taizhou City, Zhejiang Province, China. The

composition and physicochemical parameters of the groundwater are summarized in **Supplementary Table 10**. Batch experiments were conducted in this groundwater matrix using the same conditions as those employed for chlorinated hydrocarbon degradation, with the exception that HEPES buffer was replaced by the groundwater itself. Each reactor was spiked with 0.1 mM TCE, and the reaction rate was determined by fitting the TCE removal data to a pseudo-first-order kinetic model.

Continuous-Flow Column Experiment in real groundwater. A continuous-flow column reactor was designed to simulate *in situ* groundwater remediation (**Supplementary Figure 37**). The operational parameters of the column experiment were determined based on reported field groundwater-remediation experiments.[26,27] The column (15 cm length × 25 mm inner diameter) was packed with a mixture of quartz sand and $SiH^{\delta-}$-ZVI (10% $SiH^{\delta-}$-ZVI). Taizhou groundwater amended with 0.1 mM TCE and stored in a Teflon (FEP) bag was continuously pumped through the column at 0.05 m/d using a peristaltic pump, with a residence time of approximately 2.4 days. Effluent samples were periodically collected to monitor TCE concentration, assessing dechlorination efficiency and $SiH^{\delta-}$-ZVI stability under continuous-flow conditions.

Text 9: Batch experiment for trichloroacetic acid (TCAA) conversion to acetic-d_3 acid-d

In the experiment for the valorization of trichloroacetic acid (TCAA) into acetic-d_3 acid-d (AA-d_4), the reaction system was constructed as follows: A 120 mL brown glass vial was charged with 0.6 g of $SiH^{\delta-}$-ZVI material and 60 mL of deuterium oxide (D_2O), followed by the injection of a TCAA solution to a final concentration of 612 μM. The pH of the reaction system was then adjusted to 5.0 using H_2SO_4. The vial was subsequently transferred into an

anaerobic glovebox to initiate the reaction under oxygen-free conditions. Aliquot samples were taken at predetermined time points for analysis during the reaction.

After 96 hours of reaction, the mixture was processed to purify the target product, AA-d_4. The workup procedure consisted of an initial filtration of the reaction mixture, followed by distillation for separation and enrichment. The distillate was subjected to a second filtration to obtain the purified sample. Finally, the purified product was characterized by nuclear magnetic resonance (NMR, Bruker 400M) spectroscopy to confirm its chemical structure and purity.[28] NMR spectral data were analyzed using MestReNova 14.0 software.

Text 10: Theoretical calculations.

All density functional theory (DFT) calculations within the generalized gradient approximation (GGA) using the Perdew-Burke-Ernzerhof (PBE) function.[29-31] Projected augmented wave (PAW) potentials[32,33] were chosen to describe the ionic cores, using a plane wave basis set with a kinetic energy cutoff of 400 eV. Partial occupancies of the Kohn-Sham orbitals were allowed using the Gaussian smearing method with a width of 0.05 eV. The electronic energy was considered self-consistent when the energy change was smaller than 10^{-5} eV. A geometry optimization was considered convergent when the energy change was smaller than 0.03 eV $Å^{-1}$. The Brillouin zone integration is performed using 1 × 1 × 1 Monkhorst-Pack k-point sampling for a structure.

ZVI model was employed as this developed in previous studies.[34-38] The configuration of ZVI was modeled with bulk Fe (ICSD-53451) and iron oxide (ICSD-1544) surface layer, according to previous studies.[34-38] For the ZVI slab, which consist of 175 Fe atoms, 50 O atoms, the bulk structure primarily comprises metallic Fe in the lower layers, while the surface is

dominated FeO. Based on FTIR spectroscopic characterization and previous studies, the Si-ZVI structure was constructed by coordinating Na_2SiO_3 to the ZVI surface via Si–O–Fe covalent bonds in a monodentate mononuclear configuration. After geometric optimization, the Si–O bond distance of Si–O–Fe converged to 1.81 Å.

The adsorption energies (E_{ads}) of H_2, H_2O molecules on the Si-ZVI were calculated as using **Eq. S7**:

$$E_{ads} = E_{ad/sub} - E_{ad} - E_{sub} \quad \text{(S7)}$$

where $E_{ad/sub}$, E_{ad}, and E_{sub} are the total energies of the optimized adsorbate/substrate system, the adsorbate in the structure, and the clean substrate, respectively.

The Gibbs free energy of the reactant, intermediates, and products in H_2 heterolytic reduction on Si-ZVI was calculated using **Eq. S8**:

$$G = E_{ads} + \mathrm{ZPE} - \mathrm{TS} \quad \text{(S8)}$$

where G, E_{ads}, ZPE and TS are Gibbs free energy, total energy from DFT calculations, zero-point energy, and entropic contributions, respectively.

Transition states for elementary reaction steps of H_2 heterolytic reduction on Si-ZVI as well as FF reductive dechlorination and $H^{\delta-}$ regeneration on $SiH^{\delta-}$-ZVI were determined by a combination of the nudged elastic band (NEB) method and the dimer method.[39] In the NEB method, the path between the reactant and product is d is discretized into a series of structural images. The image that is closest to a likely transition state structure was then employed as an initial guess structure for the dimer method. All atomic structure visualization and DFT calculation data analysis were completed using VASP 6.3.2 and VESTA 3.5 software.

Supplementary Figures

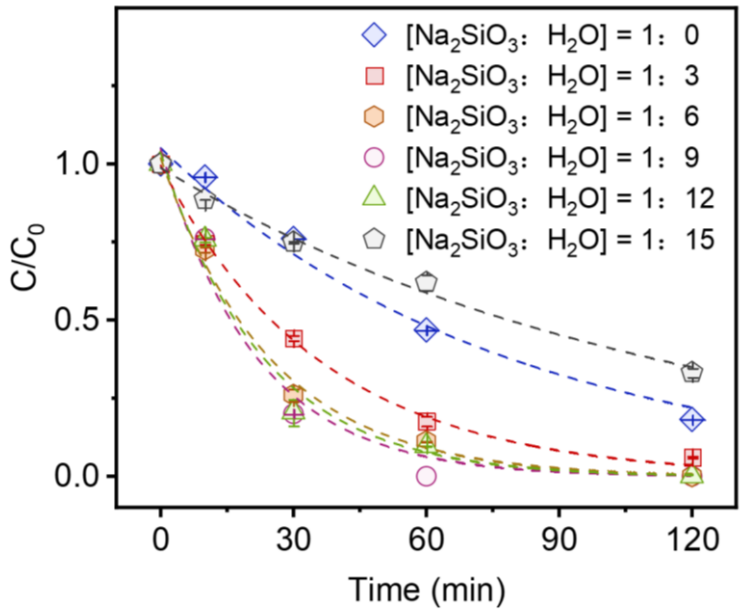

Supplementary Figure 1. Kinetics of FF degradation fitted to a first-order kinetic model by $SiH^{\delta-}$-ZVI under different volume of water. All measurements were performed in triplicate (n=3 independent experiments). Reaction conditions: ZVI dosage = 10 $g \cdot L^{-1}$, FF = 20 ppm, 50 mM HEPES, pH 7, anoxic, T = 25 °C.

The volume of deionized water added as H source was systematically optimized. Samples prepared with 0, 23, 46, 69, 92 and 115 μL water, corresponding to the Na_2SiO_3: H_2O molar ratio ranging from 1:0 to 1:15, were evaluated based on their performance in FF degradation. The $SiH^{\delta-}$-ZVI synthesized with 69 μL exhibited the highest FF degradation activity; therefore, this volume was selected as optimal for subsequent material characterization and experiments.

Supplementary Figure 2. Experimental process for hydrogen content detection in mechanochemical synthesis.

The experimental procedure for hydrogen quantification during mechanochemical synthesis comprised three sequential steps: mechanochemical synthesis, gas extraction, and gas chromatographic analysis. Mechanochemical synthesis was conducted in a sealed batch ball milling reactor. Gas extraction was performed using a gas-tight syringe to withdraw hydrogen from the vacuum tank. The extracted sample was then analyzed using gas chromatography to determine the hydrogen concentration.

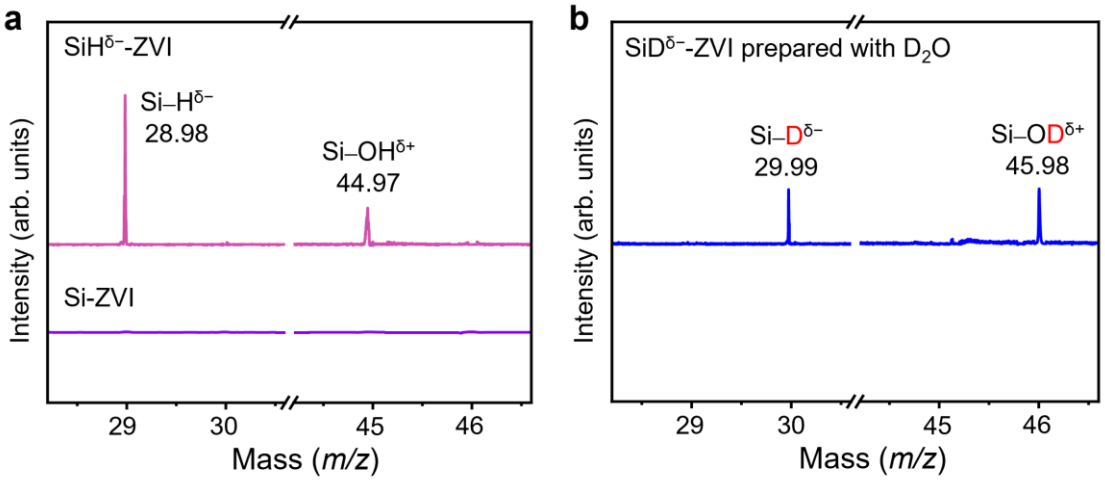

384

385 **Supplementary Figure 3.** The TOF-SIMS spectra of **a.** SiH$^{\delta-}$-ZVI and Si-ZVI, and **b.** SiD$^{\delta-}$-

386 ZVI prepared by D_2O.

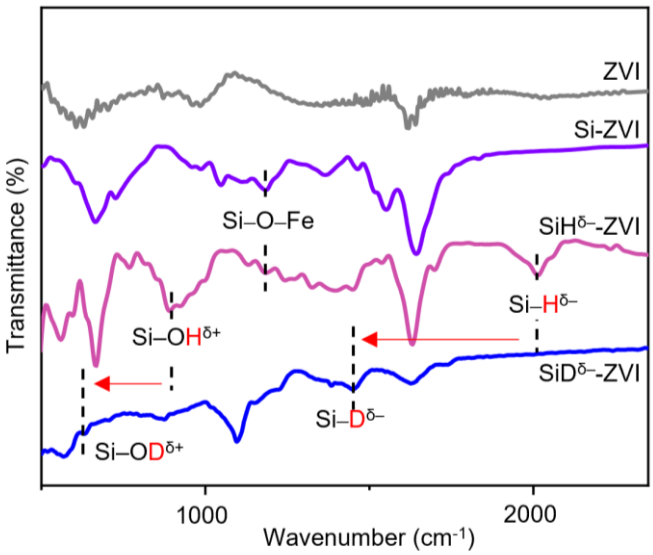

387

388 **Supplementary Figure 4.** FTIR spectra of ZVI, Si-ZVI, $SiH^{\delta-}$-ZVI and $SiD^{\delta-}$-ZVI.

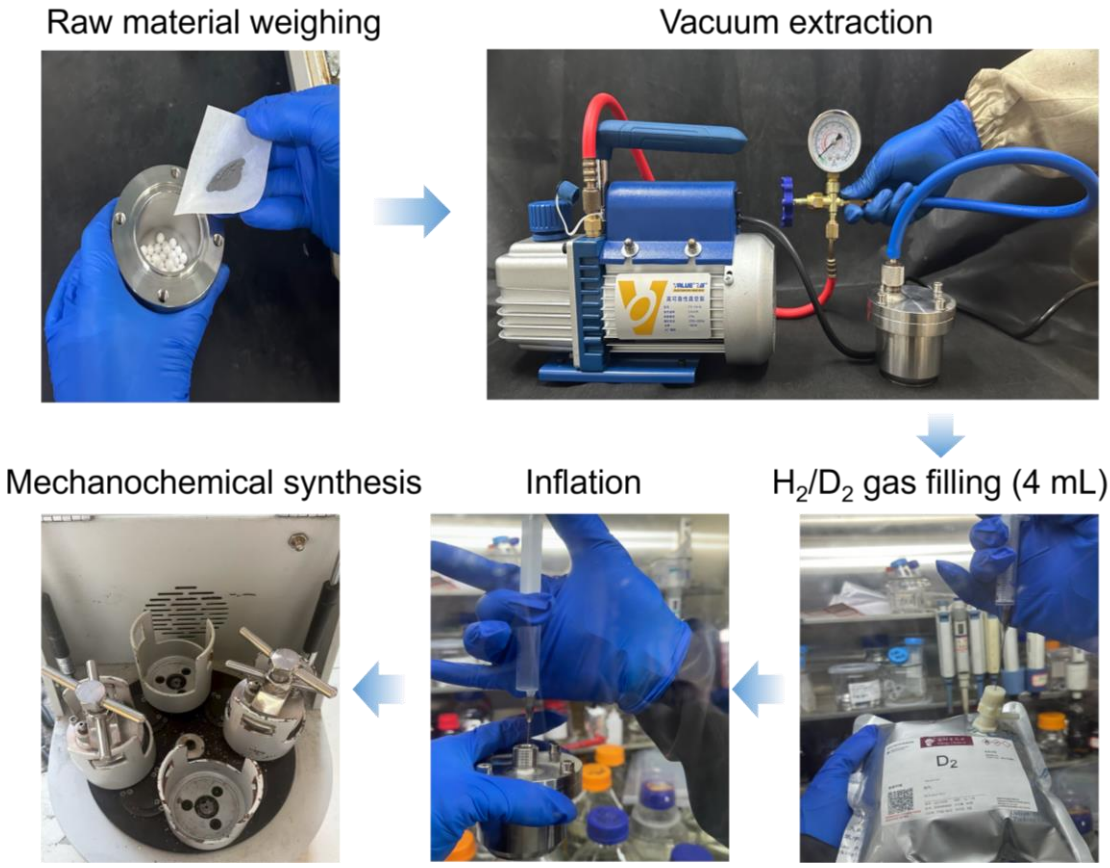

Supplementary Figure 5. Preparation of $SiH^{\delta-}$-ZVI(H_2) and $SiD^{\delta-}$-ZVI(D_2) using H_2 and D_2 as the proton source for silicon-hydride synthesis

$SiH^{\delta-}$-ZVI and $SiD^{\delta-}$-ZVI were synthesized via mechanochemical ball milling under H_2 or D_2 atmosphere, respectively. Briefly, predetermined amounts of reduced iron powder and sodium silicate were loaded into a sealed milling jar. The jar was evacuated using a vacuum pump, followed by the introduction of 4 mL of H_2 or D_2 gas. Ball milling was then conducted under the corresponding gas atmosphere to obtain $SiH^{\delta-}$-ZVI or $SiD^{\delta-}$-ZVI.

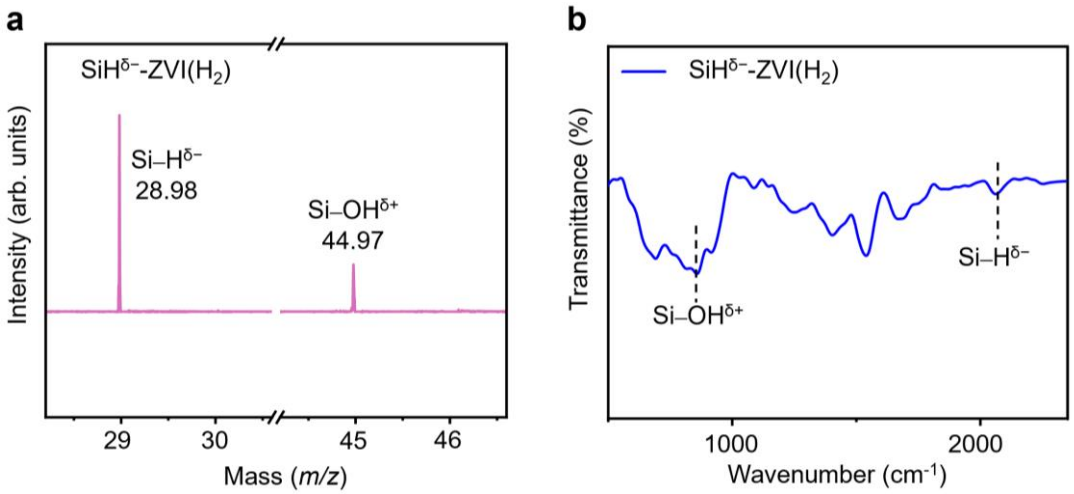

397

398 **Supplementary Figure 6. a.** TOF-SIMS and **b.** FTIR spectra of SiH$^{\delta-}$-ZVI(H_2).

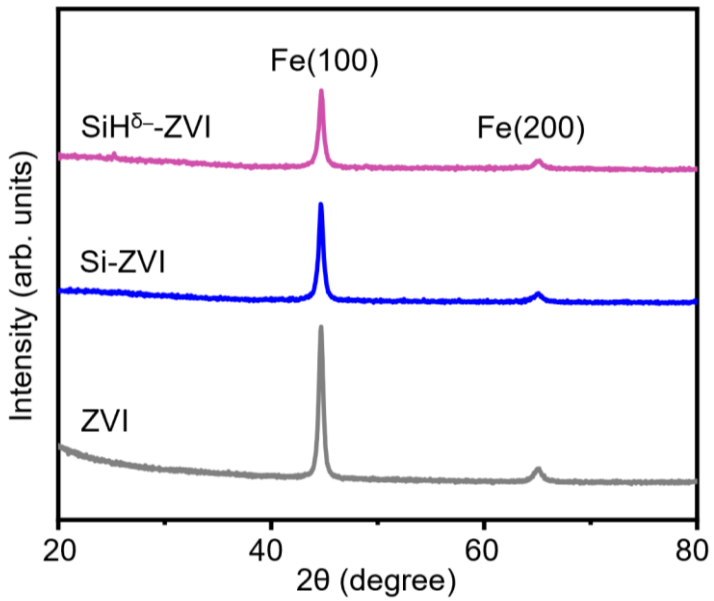

399

400 **Supplementary Figure 7.** XRD patterns of SiH$^{\delta-}$-ZVI, Si-ZVI and ZVI.

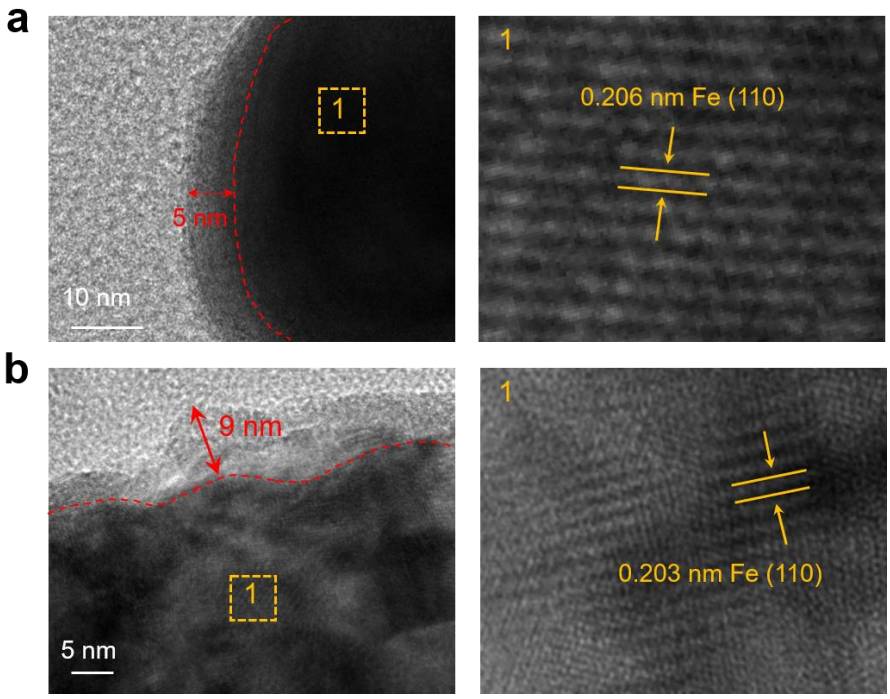

Supplementary Figure 8. HRTEM images of **a.** $SiH^{\delta-}$-ZVI, **b.** ZVI. Insets show higher-magnification views of the regions marked "1" (yellow boxes), with measured lattice spacing corresponding to the Fe (110) crystal plane.

The surface silicon hydride modification well preserves the core-shell structure of ZVI, with the oxide shell thickness decreasing from approximately 9 nm for pristine ZVI to 5 nm for $SiH^{\delta-}$-ZVI.

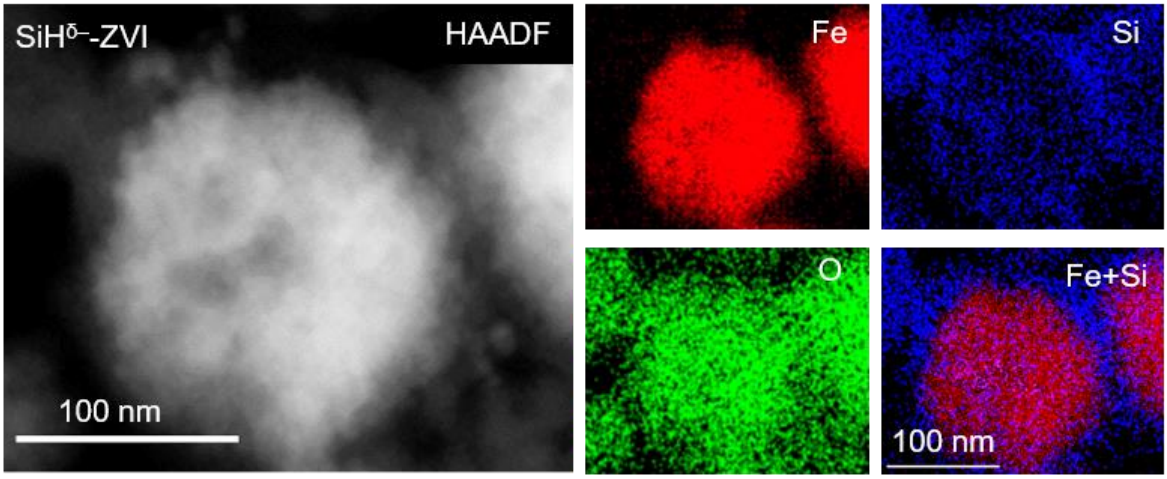

409

410 **Supplementary Figure 9.** HAADF-STEM elemental mapping of SiH$^{\delta-}$-ZVI: HAADF

411 micrograph, Fe/Si/O distribution, and Fe-Si overlay.

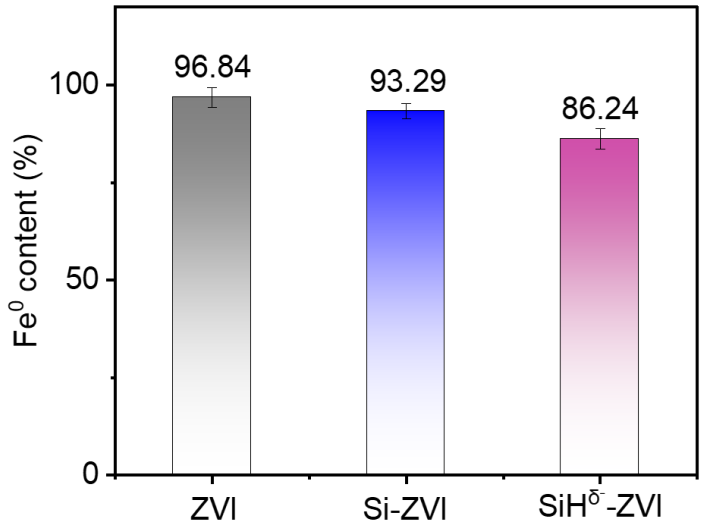

412

413 **Supplementary Figure 10.** Fe^0 content of ZVI, Si-ZVI, and $SiH^{\delta-}$-ZVI. All measurements

414 were performed in

415 triplicate (n=3 independent experiments).

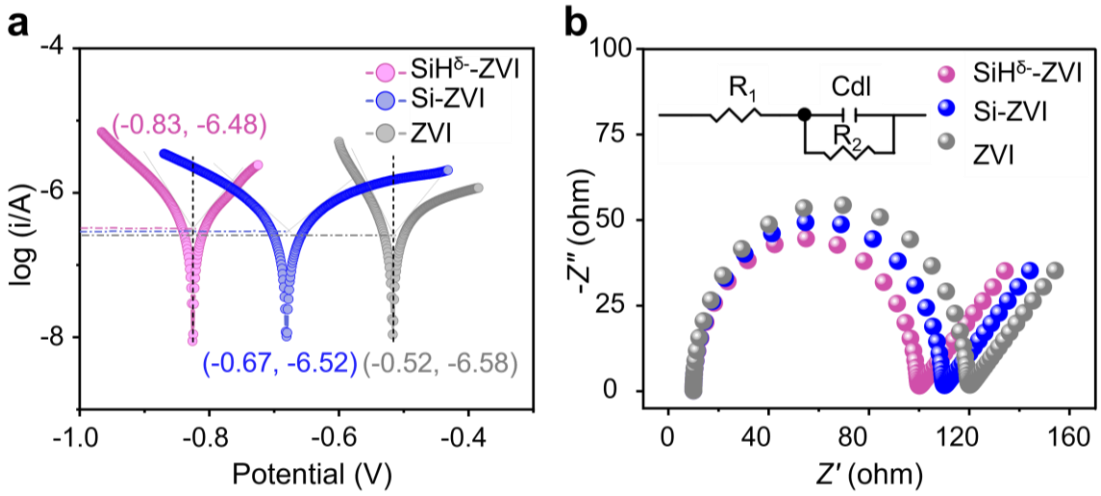

Supplementary Figure 11. Electrochemical Characterization of $SiH^{\delta-}$-ZVI, Si-ZVI, and ZVI. **a.** Tafel polarization curves; **b.** Nyquist plots fitted to an equivalent circuit model comprised of electrolyte resistance (Rs), charge transfer and contact resistance (Rct) and a constant phase element (CPE).

Electrochemical characterization was used to investigate the effect of $SiH^{\delta-}$ modification on the electron transfer properties of ZVI. Tafel polarization curve analysis shows that $SiH^{\delta-}$-ZVI had the lowest corrosion potentials (approximately -0.83 V vs. -0.63 V for Si-ZVI; -0.83 V vs. -0.52 V for ZVI) and higher corrosion currents (approximately 0.33 μA vs. 0.30μA for Si-ZVI; 0.33 μA vs. 0.26 μA for ZVI) compared with that of ZVI and Si-ZVI. Meanwhile, EIS showed that $SiH^{\delta-}$-ZVI had a lower charge transfer resistance (100 Ω) compared to Si-ZVI (110 Ω) and ZVI (120 Ω). These results collectively confirm that $SiH^{\delta-}$ modification could facilitate electron emission and interfacial transfer of ZVI.

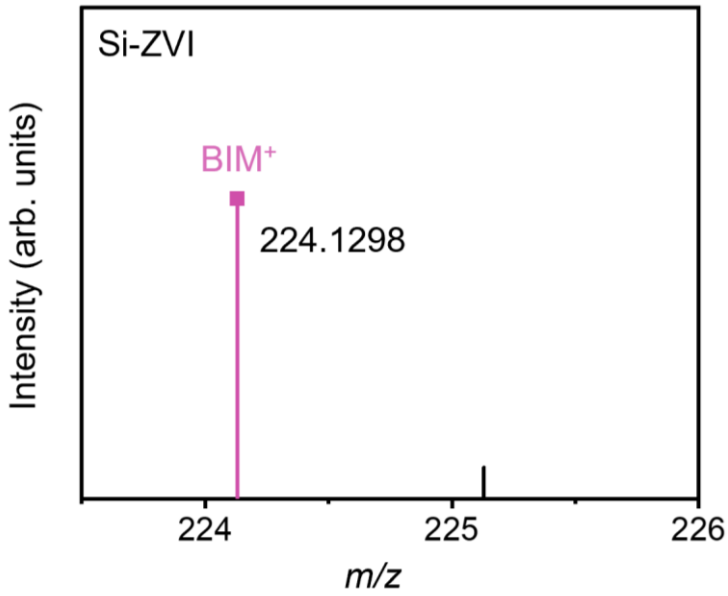

Supplementary Figure 12. Mass spectrometry data for BIM^+ hydrogenation by Si-ZVI.

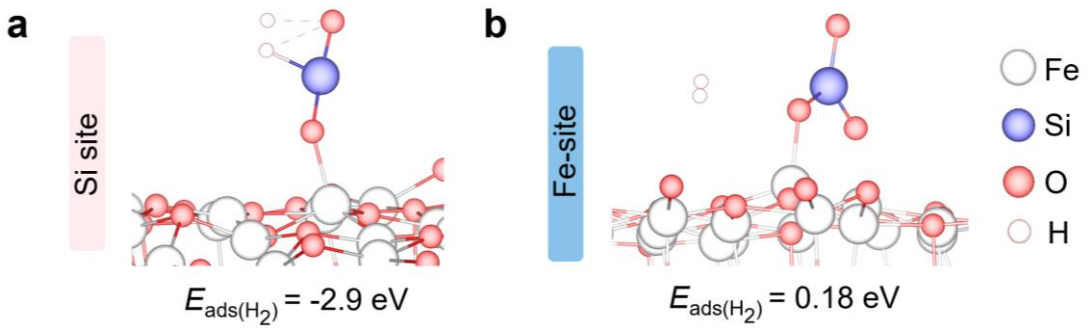

Supplementary Figure 13. H_2 adsorption configurations on **a.** Si, and **b.** Fe sites on Si-ZVI and the corresponding adsorption energies (E_{ads}).

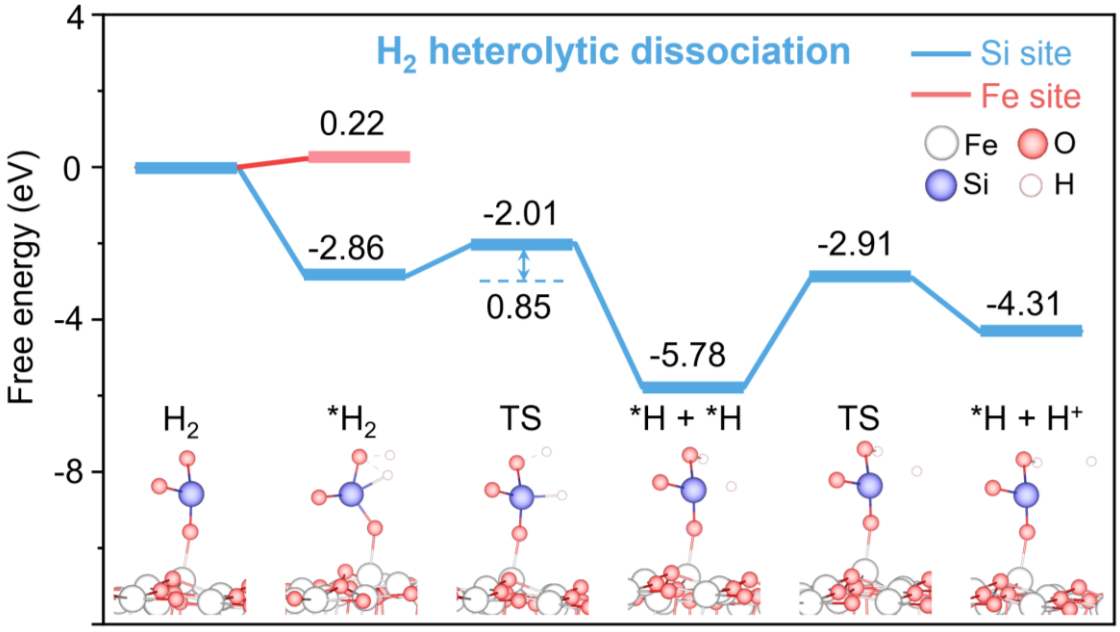

435

436 **Supplementary Figure 14.** Energy profiles of heterolytic H_2 dissociation on Si-ZVI, inclusive

437 of side-view geometries of initial, transition (TS), and final States.

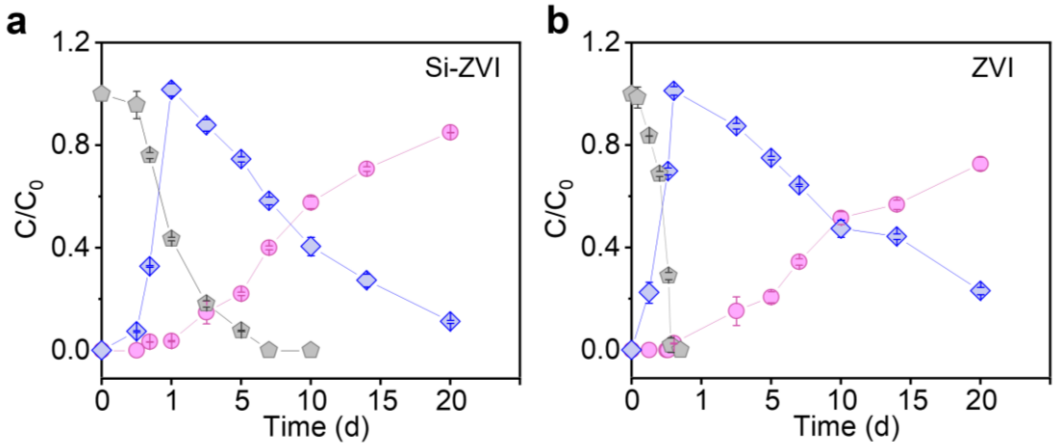

438

439 **Supplementary Figure 15.** Kinetics of FF disappearance and formation of degradation

440 products by **a.** Si-ZVI and **b.** ZVI. (●) FF; (●) dFF; (●) ddFF. All measurements were

441 performed in triplicate (n=3 independent experiments). Reaction conditions: Fe^0 =10

442 $g \cdot L^{-1}$, FF = 20 ppm, 50 mM HEPES, pH 7, anoxic, T = 25 °C.

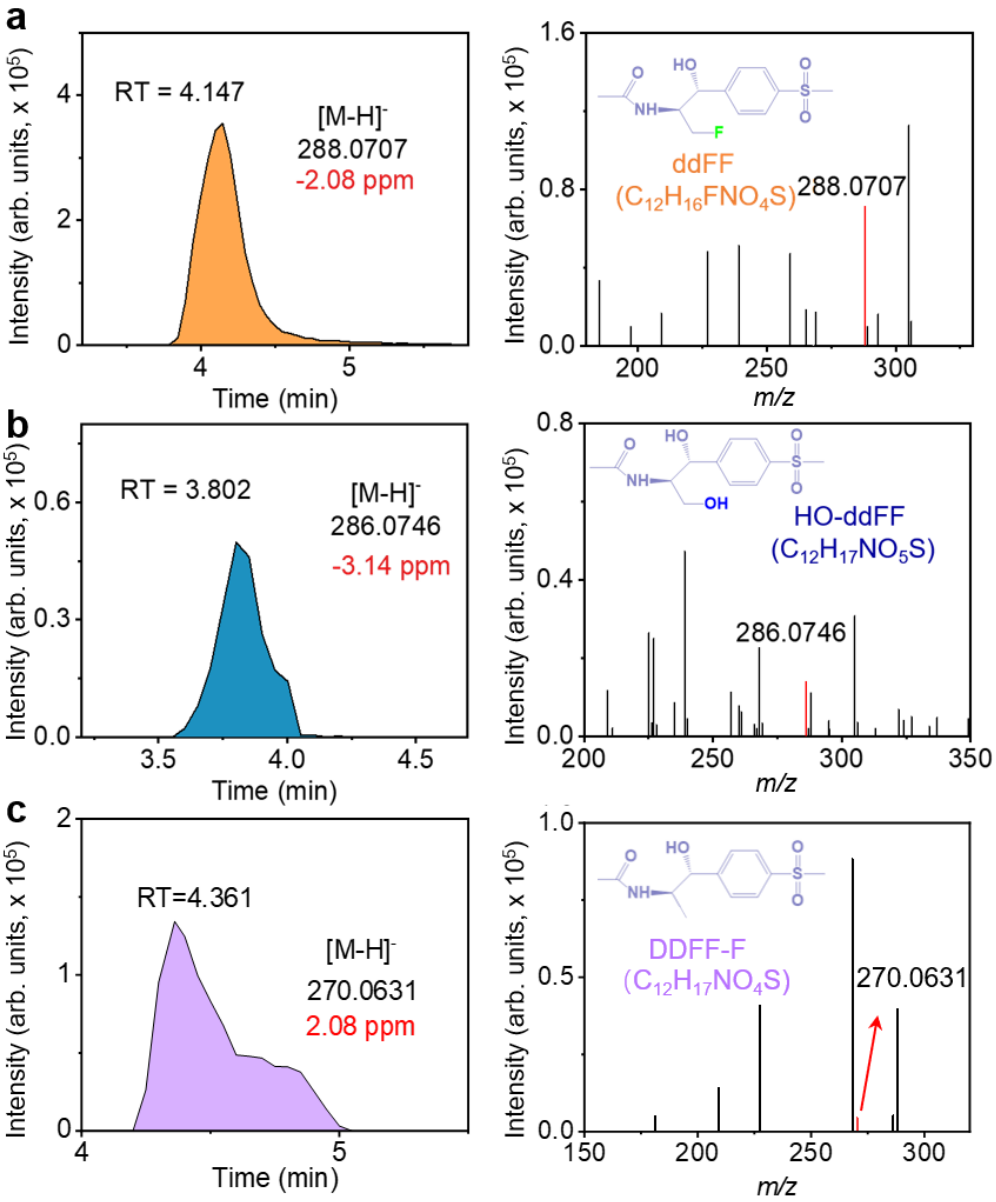

443

444 **Supplementary Figure 16.** HPLC-MS/MS analysis of FF degradation products by

445 $SiH^{\delta-}$-ZVI (20-day reaction). Chromatograms and corresponding MS^2 spectra of **a.**

446 dechlorinated FF (ddFF); **b.** the hydrolysis defluorination product of ddFF (HO-ddFF);

447 **c.** the defluorination product of ddFF (ddFF-F). Right insets: Corresponding MS^2

448 spectra.

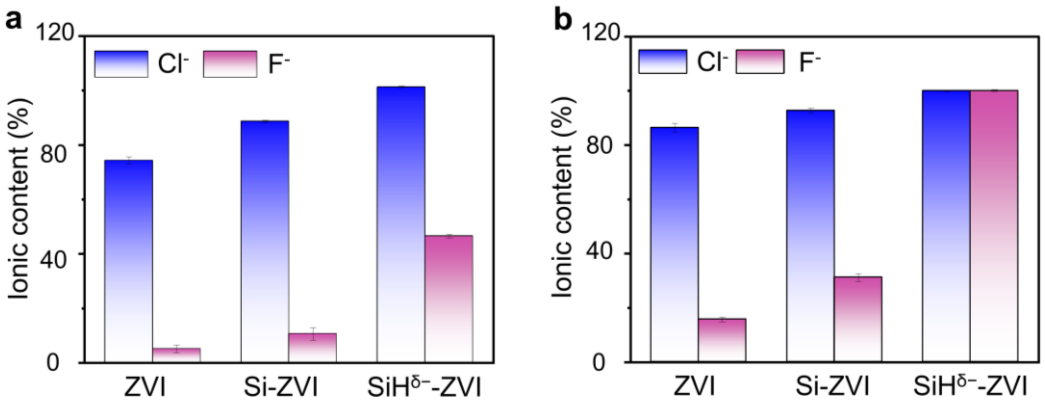

Supplementary Figure 17. Cl^- and F^- released during FF degradation by the ZVIs: **a.** after 20 days; **b.** after 40 days of reaction. All measurements were performed in triplicate (n=3 independent experiments). Data are presented as the mean ± standard deviation. Reaction conditions: Fe^0 = 10 $g \cdot L^{-1}$, FF = 20 ppm, 50 mM HEPES, pH 7, anoxic, T = 25 °C.

$SiH^{\delta-}$-ZVI achieves 100% dechlorination and defluorination efficiency for FF degradation after 40 days of reaction. The complete dehalogenation confirms that the cleaved halide species do not accumulate on the material surface, and thus cause no active site poisoning or blocking.

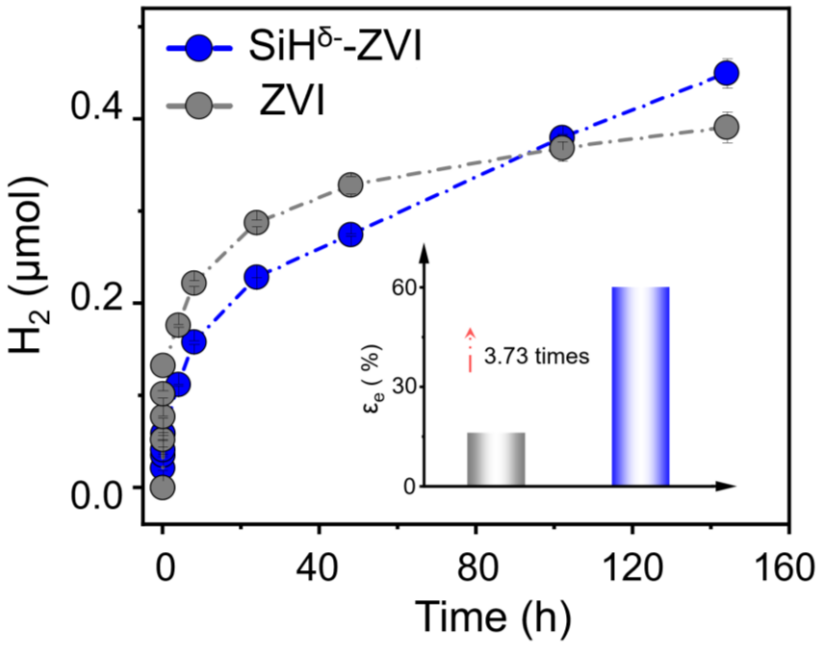

460

461 **Supplementary Figure 18**. H_2 evolution during FF degradation by $SiH^{\delta-}$-ZVI and ZVI.

462 All measurements were performed in triplicate (n=3 independent experiments). Data

463 are presented as the mean ± standard deviation. Inset: Electron efficiency (ε_e) of the

464 ZVIs toward FF degradation.

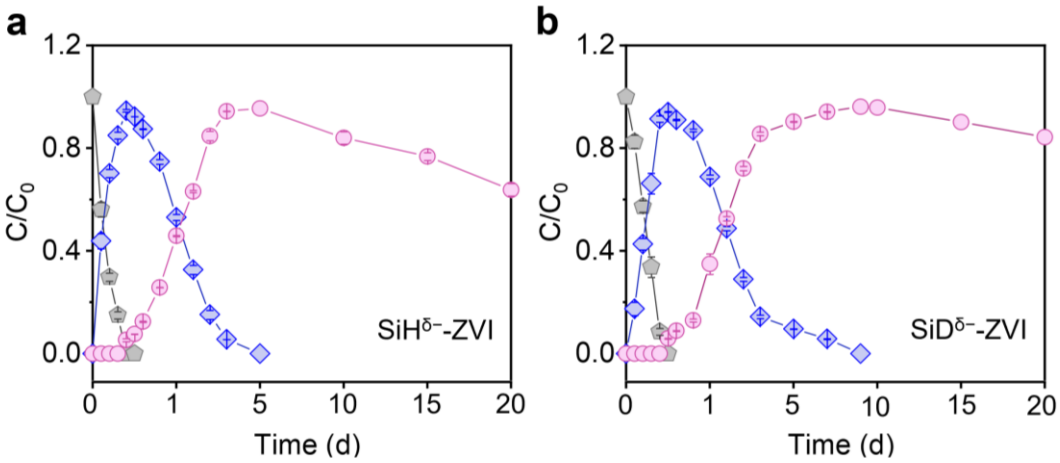

Supplementary Figure 19. Kinetics of FF disappearance and formation of degradation products in FF degradation by a. $SiH^{\delta-}$-ZVI and b. $SiD^{\delta-}$-ZVI. (●) FF; (●) dFF; (●) ddFF. All measurements were performed in triplicate (n=3 independent experiments). Data are presented as the mean ± standard deviation. Reaction conditions: Fe^0 = 10 g·L^{-1}, FF = 20 ppm, 50 mM HEPES, pH 7, anoxic, T = 25 °C.

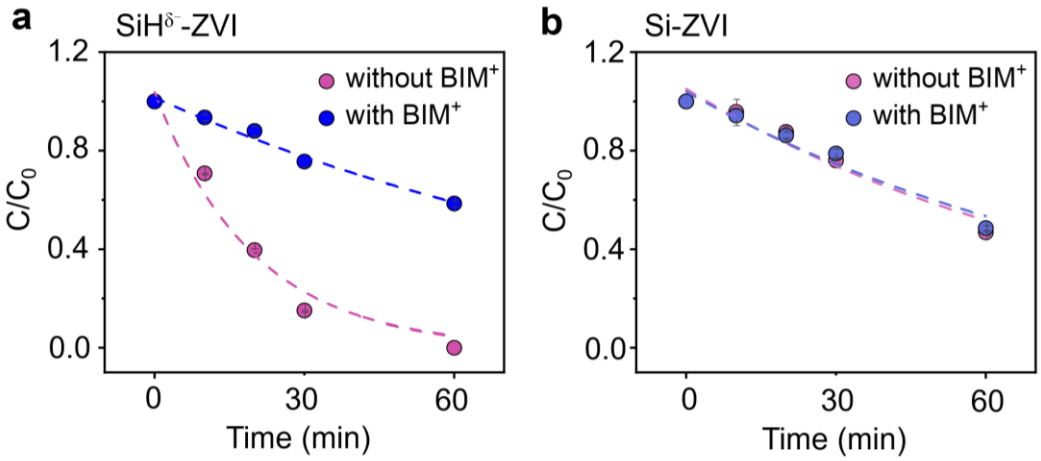

471

472 **Supplementary Figure 20.** Kinetics of FF degradation by **a.** $SiH^{\delta-}$-ZVI, and **b.** Si-ZVI

473 with addition of BIM^+ ([BIM^+] = 0.4 mM). All measurements were performed in

474 triplicate (n=3 independent experiments). Data are presented as the mean ± standard

475 deviation. Reaction conditions: Fe^0 = 10 g·L^{-1}, FF = 20 ppm, 50 mM HEPES, pH 7,

476 anoxic, T = 25 °C.

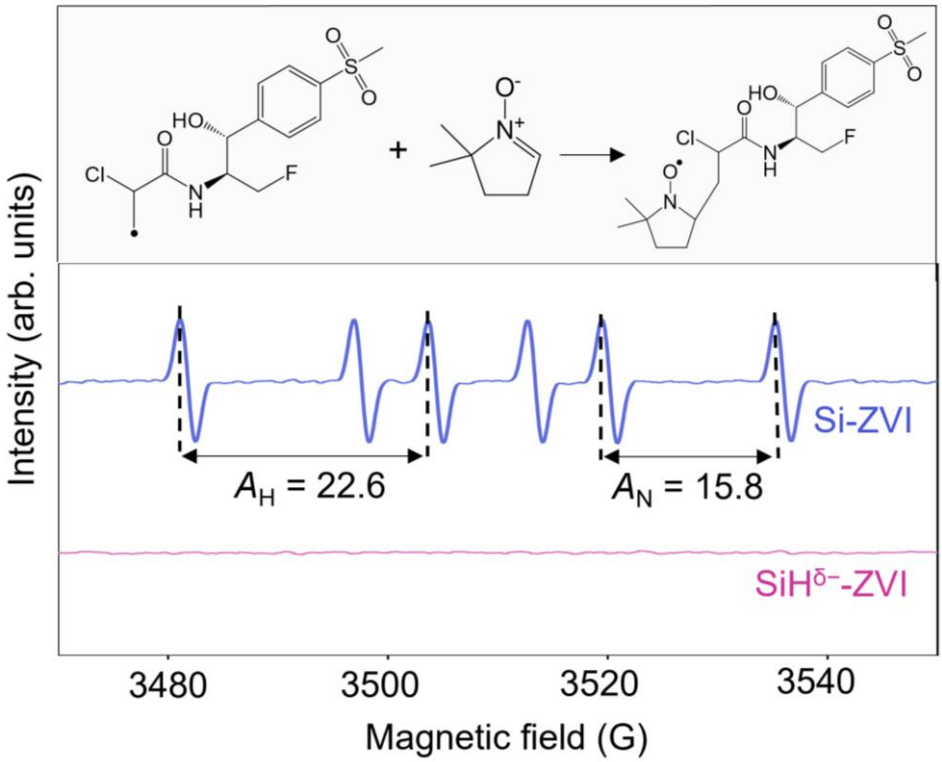

477

478 **Supplementary Figure 21.** Electron paramagnetic resonance (EPR) analysis of dFF•

479 in FF degradation by SiH$^{\delta-}$-ZVI and Si-ZVI with DMPO ([DMPO] = 100 mmol·L^{-1})

480 as the spin-trapping agent.

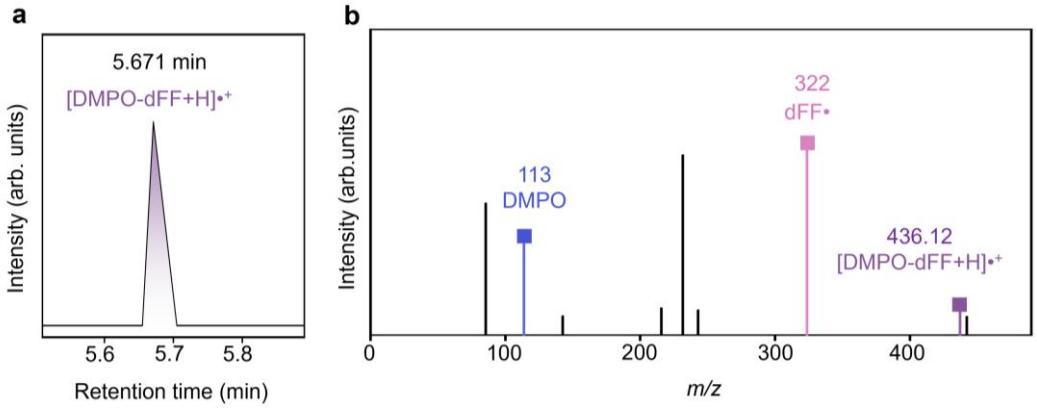

481

482 **Supplementary Figure 22.** The identification of the carbon-centered radical

483 intermediate generated during the FF degradation by Si-ZVI using DMPO ([DMPO] =

484 100 mmol·L^{-1}) as the spin-trapping agent, as evidenced by **a.** UHPLC/ESI-MS

485 chromatograph, and **b.** the associated MS^2 spectrum of protonated adduct ion [DMPO-

486 dFF + H]•$^+$.

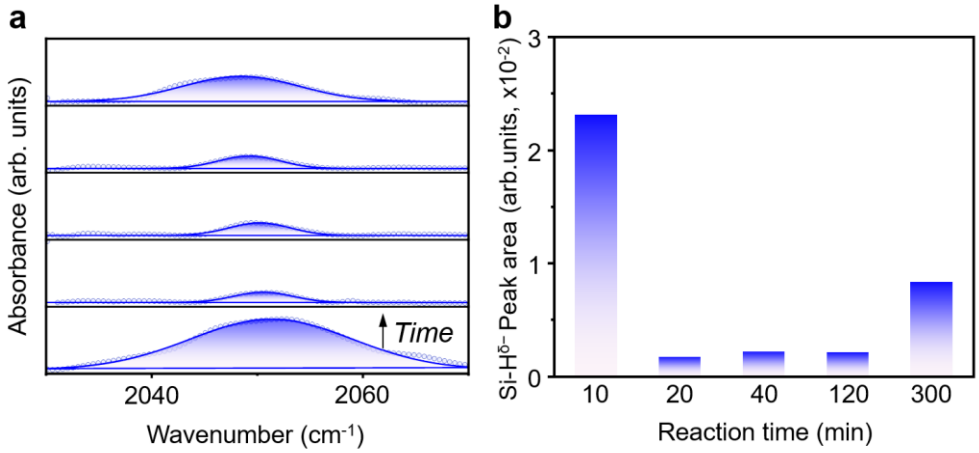

Supplementary Figure 23. a. Time-dependent integrated peak area, and **b.** temporal variation of absolute peak area of the Si–$H^{\delta-}$ characteristic band at 2052 cm^{-1} derived from *in-situ* FTIR spectra during FF degradation by $SiH^{\delta-}$-ZVI (**Fig. 3g**).

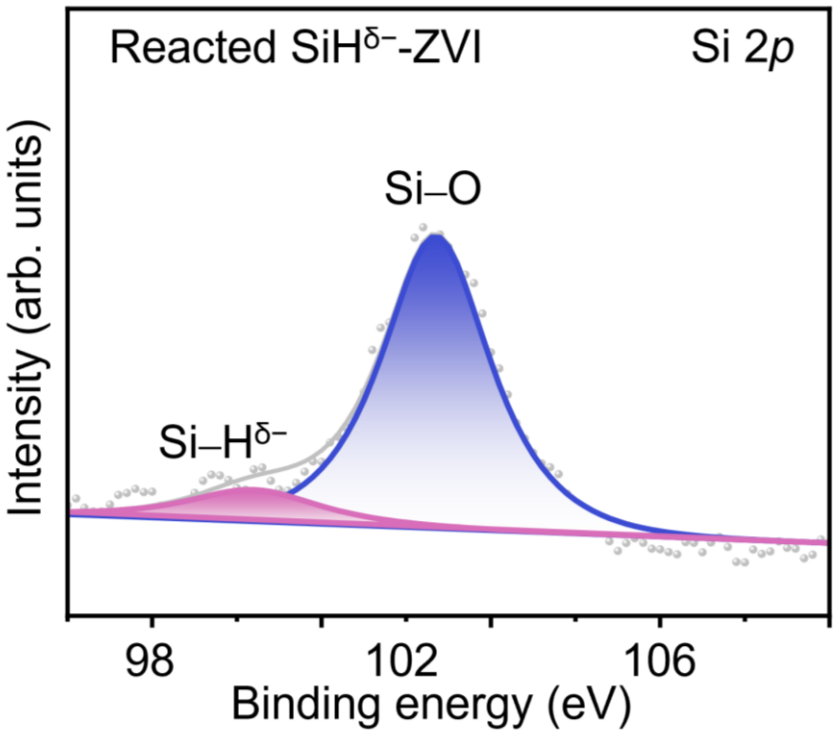

Supplementary Figure 24. Si 2*p* XPS spectra of reacted SiH$^{\delta-}$-ZVI after SiH$^{\delta-}$-ZVI reaction with FF in H_2O for 1 h (reacted SiH$^{\delta-}$-ZVI$_{(H_2O\text{-}FF)}$).

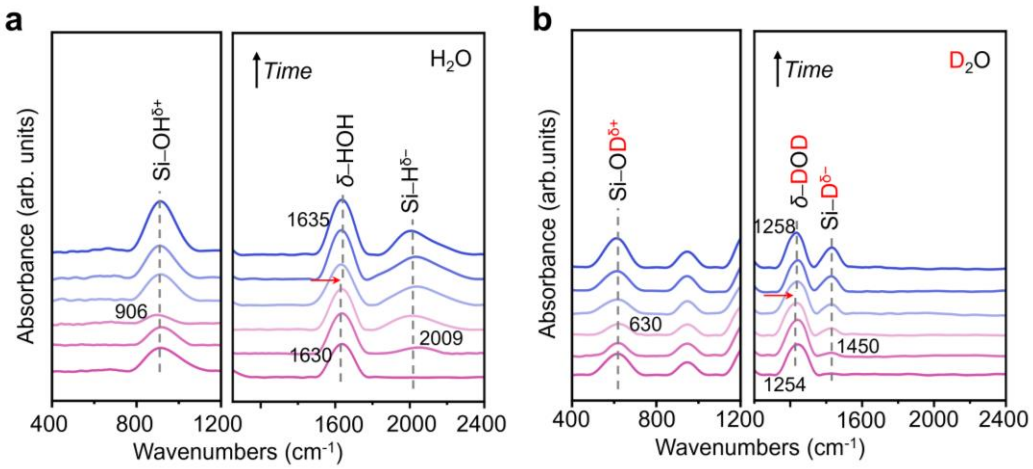

Supplementary Figure 25. *In situ* FTIR spectra of **a.** the reacted $SiH^{\delta-}$-$ZVI_{(H_2O\text{-}FF)}$ and **b.** the reacted $SiH^{\delta-}$-$ZVI_{(D_2O\text{-}FF)}$ regenerated in H_2O and D_2O, respectively.

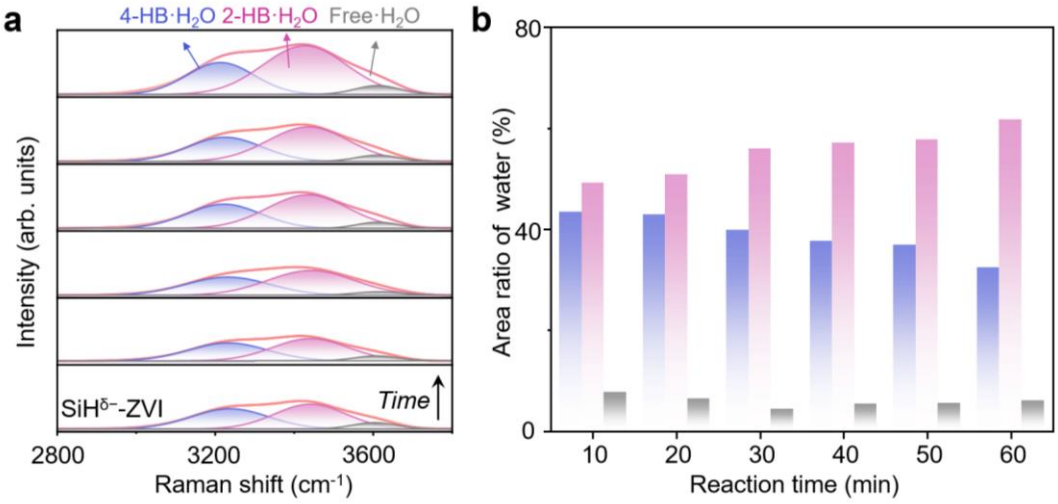

497

498 **Supplementary Figure 26. a.** Raman spectra of $SiH^{\delta-}$-ZVI and **b.** the area ratios of 2-

499 HB·H_2O, 4-HB·H_2O, and free water at different reaction times (10, 20, 30, 40, 50, and

500 60 min).

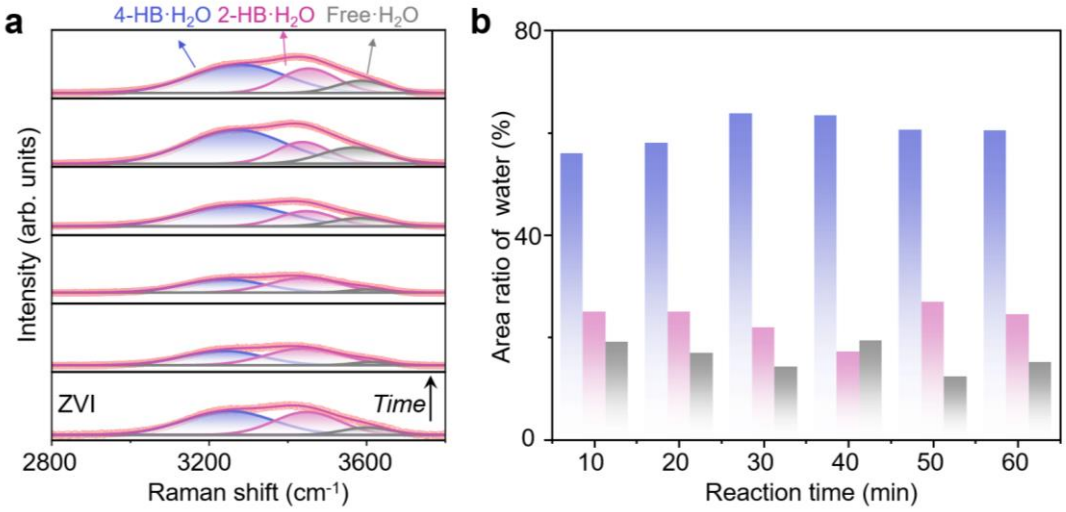

501

502 **Supplementary Figure 27. a.** Raman spectra of ZVI and **b.** the area ratios of 2-

503 HB·H_2O, 4-HB·H_2O, and free water at different reaction times (10, 20, 30, 40, 50, and

504 60 min).

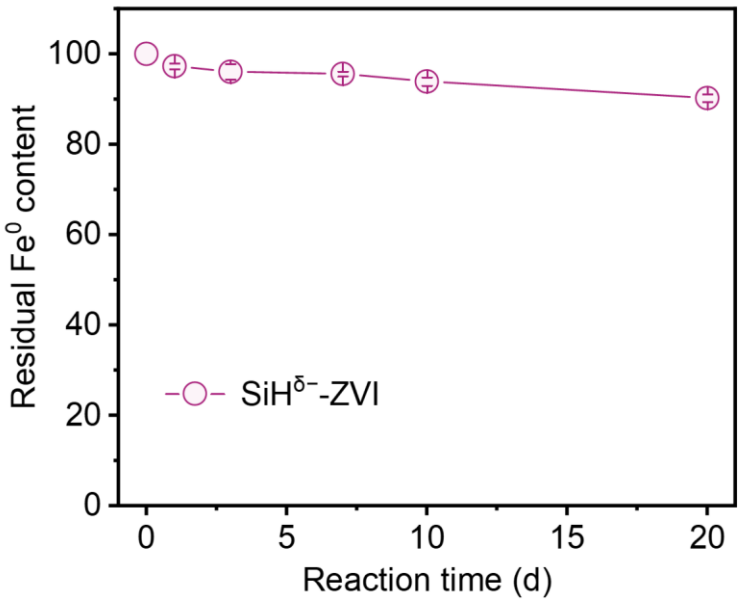

505

506 **Supplementary Figure 28**. Variation of residual Fe^0 content in $SiH^{\delta-}$-ZVI during FF

507 degradation. All measurements were performed in triplicate (n=3 independent

508 experiments). Data are presented as the mean ± standard deviation. Reaction conditions:

509 Fe^0 = 10 g·L^{-1}, FF = 20 ppm, 50 mM HEPES, pH 7, anoxic, T = 25 °C.

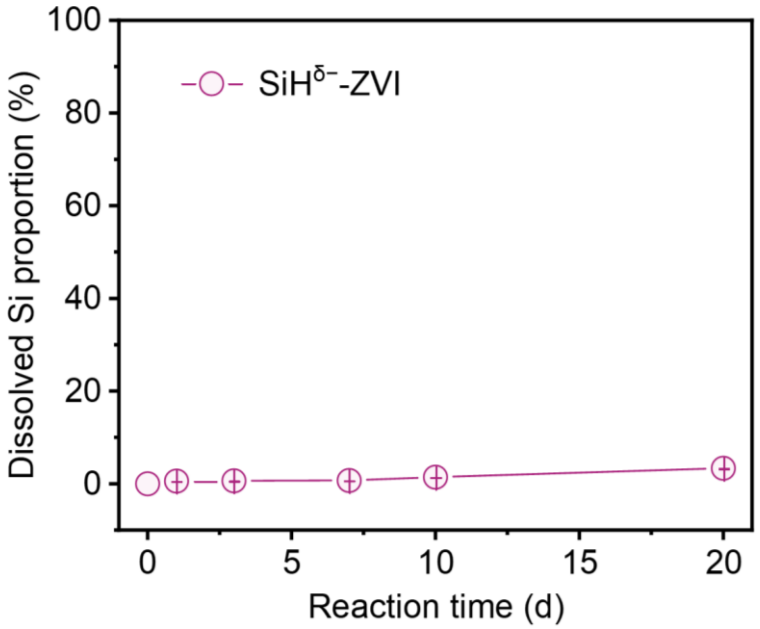

510

511 **Supplementary Figure 29.** Cumulative Si leaching percentage relative to total initial
512 Si content of SiH$^{\delta-}$-ZVI during FF degradation. All measurements were performed in
513 triplicate (n=3 independent experiments). Data are presented as the mean ± standard
514 deviation. Reaction conditions: Fe^0 = 10 g·L^{-1}, FF = 20 ppm, 50 mM HEPES, pH 7,
515 anoxic, T = 25 °C.

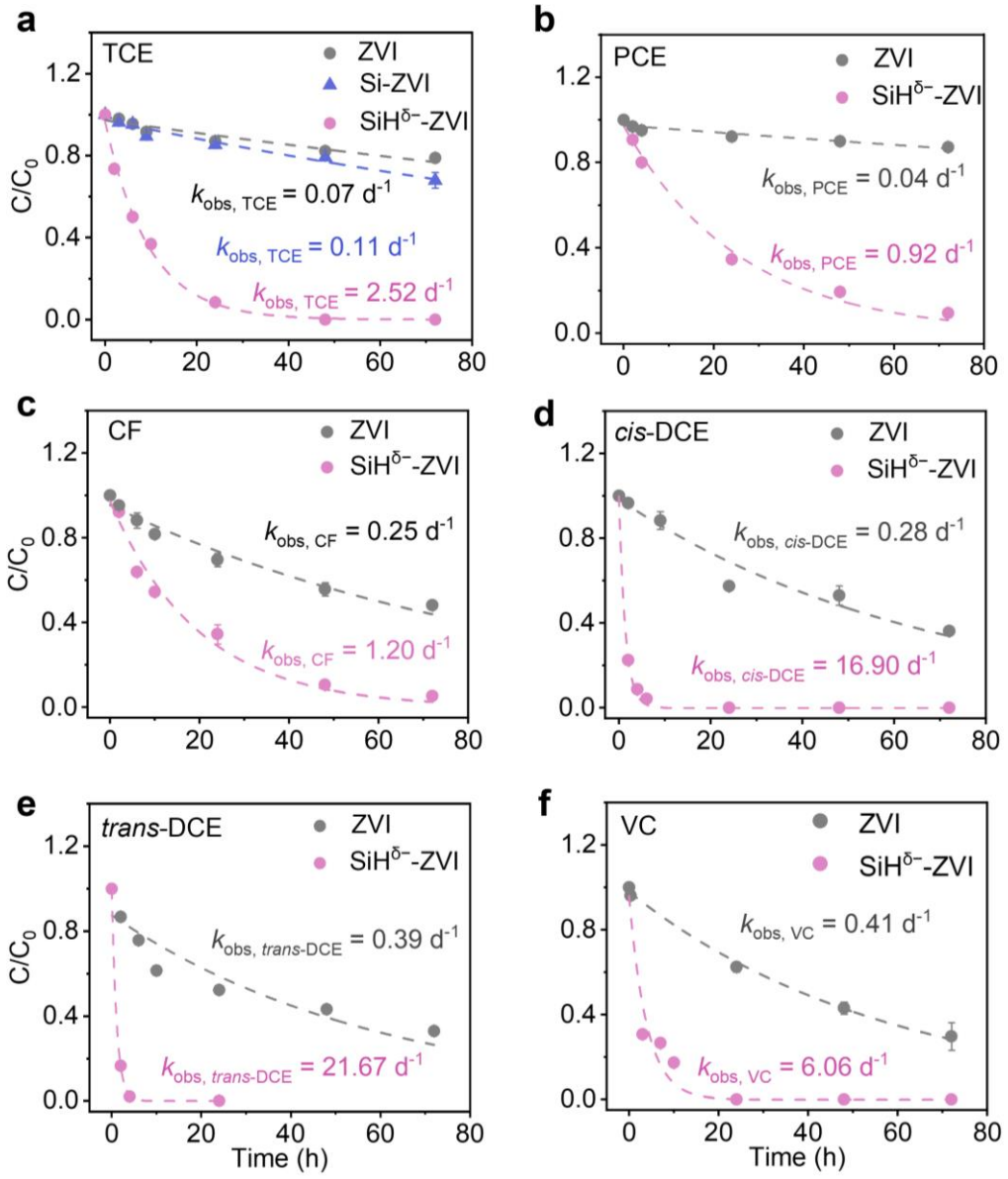

Supplementary Figure 30. Degradation kinetics of chlorinated carbons by SiH$^{\delta-}$-ZVI and ZVI fitted to a first-order kinetic model. **a.** TCE, **b.** PCE, **c.** CF, **d.** *cis*-DCE, **e.** *trans*-DCE, **f.** VC. All measurements were performed in triplicate (n=3 independent experiments). Data are presented as the mean ± standard deviation. Reaction conditions: [Fe] = 10 g·L^{-1}, [CHCs] = 100 μM, 50 mM HEPES buffer, pH 7.0, anoxic conditions, T = 25 °C.

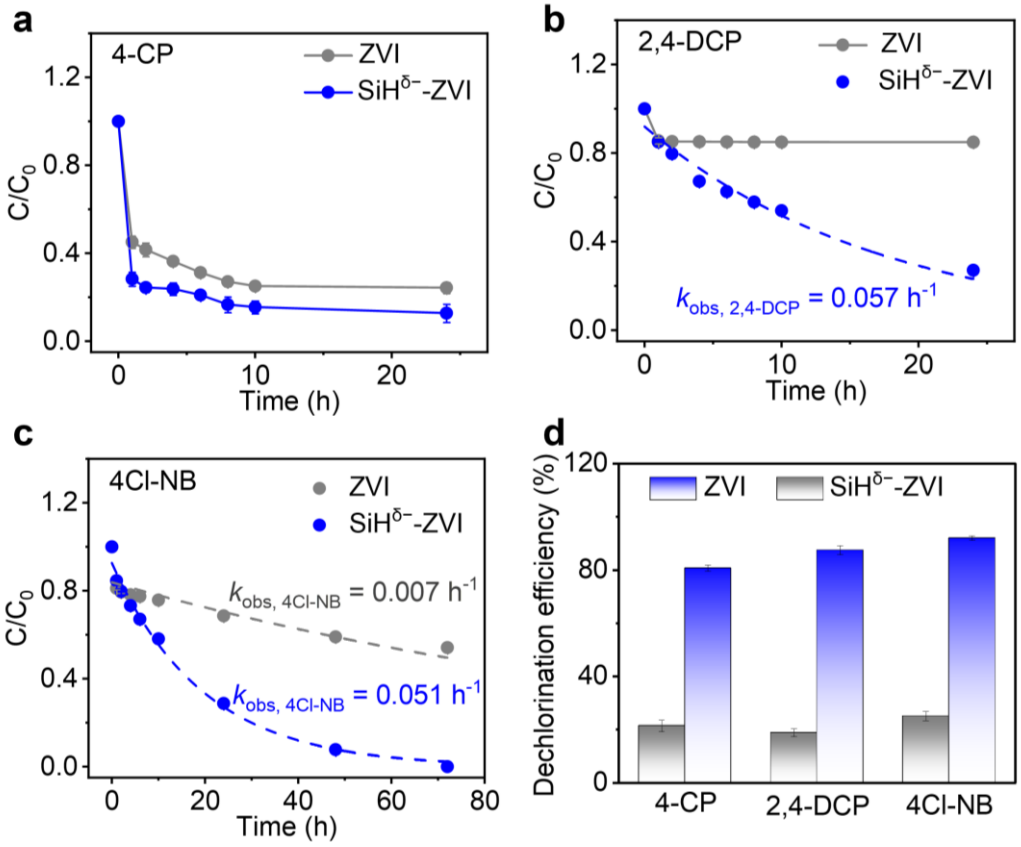

Supplementary Figure 31. Degradation kinetics of other chlorinated carbons, including **a.** 2,4-dichlorophenol (2,4-DCP), **b.** 4-chlorophenol (4-CP), and **c.** 4-chloronitrobenzene (4Cl-NB), by ZVI and SiH$^{\delta-}$-ZVI fitted to a first-order kinetic model. **d.** Percent dechlorination of chlorinated carbons by ZVI and SiH$^{\delta-}$-ZVI. All measurements were performed in triplicate (n=3 independent experiments). Data are presented as the mean ± standard deviation. Reaction conditions: [Fe] = 10 g·L^{-1}, [aromatic pollutants] = 100 μM, 50 mM HEPES buffer, pH 7.0, anoxic conditions, T = 25 °C.

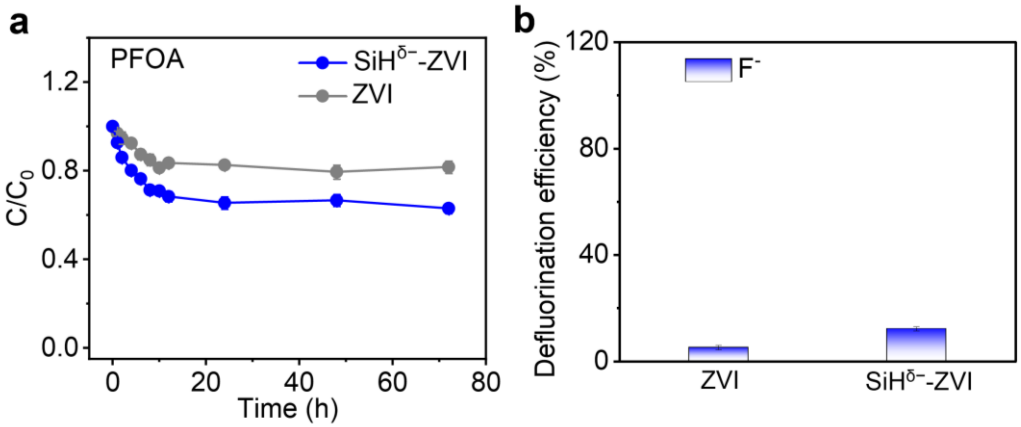

532

533 **Supplementary Figure 32**. **a.** Degradation of PFOA by SiH$^{\delta-}$-ZVI. **b.** Corresponding
534 defluorination efficiency. All measurements were performed in triplicate (n=3
535 independent experiments). Data are presented as the mean ± standard deviation.
536 Reaction conditions: Fe^0 = 10 g·L^{-1}, PFOA = 20 ppm, 50 mM HEPES, pH 7, anoxic, T
537 = 25 °C.

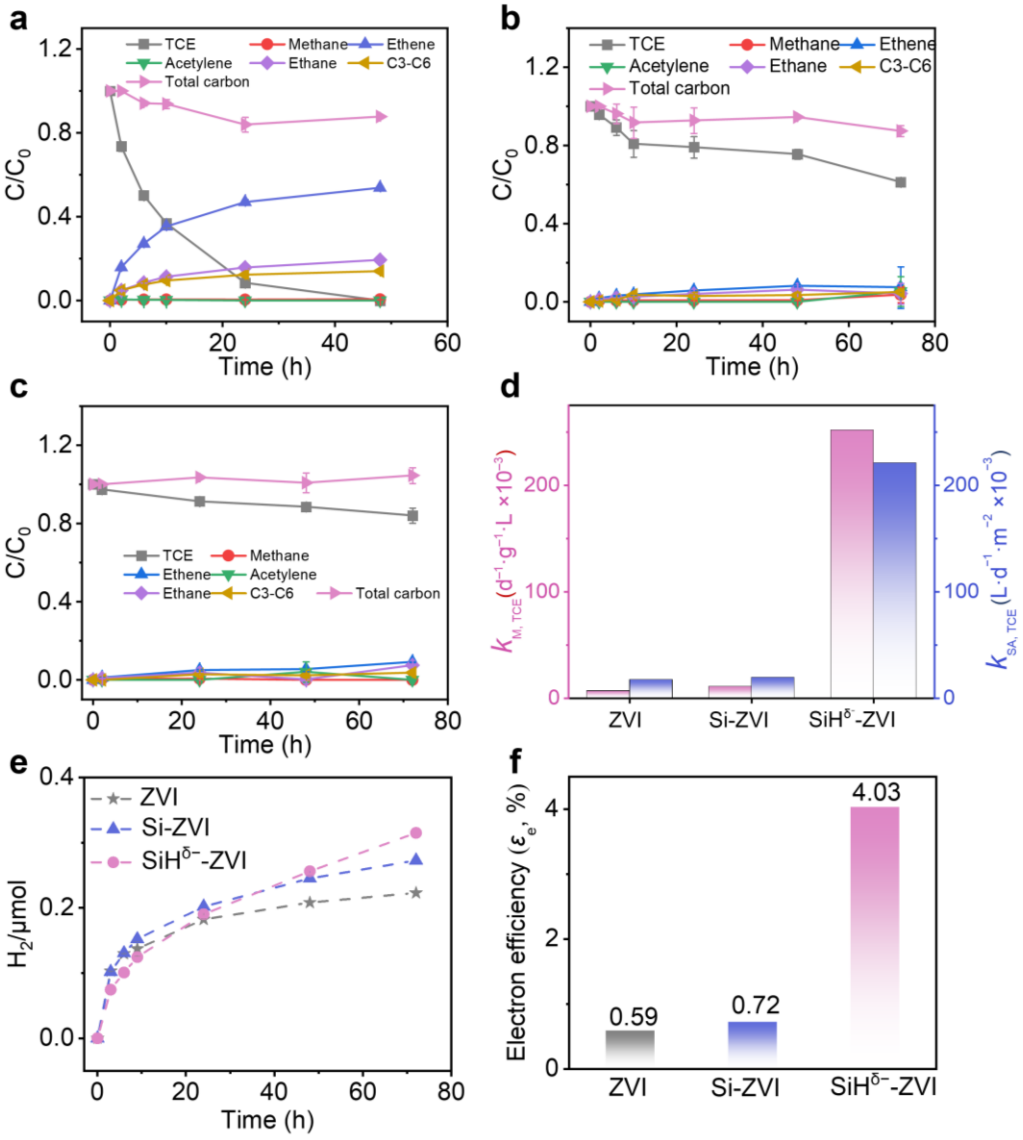

Supplementary Figure 33. Kinetics of TCE dechlorination and formation of major products by **a.** $SiH^{\delta-}$-ZVI, **b.** Si-ZVI, and **c.** ZVI. **d.** Values of surface area normalized rate constants. **e.** HER activity of $SiH^{\delta-}$-ZVI, Si-ZVI, and ZVI. **f.** Electron efficiency (ε_e) for TCE dechlorination by $SiH^{\delta-}$-ZVI, Si-ZVI, and ZVI. All measurements were performed in triplicate (n=3 independent experiments). Data are presented as the mean ± standard deviation. Reaction conditions: [Fe] = 10 $g \cdot L^{-1}$, [TCE] = 100 μM, 50 mM HEPES buffer, pH 7.0, under anoxic conditions, T = 25 °C.

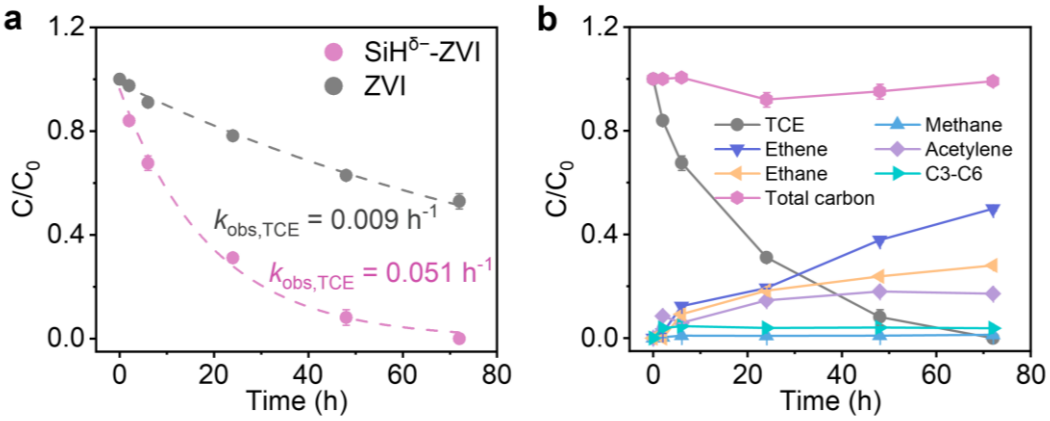

Supplementary Figure 34. Comparison of TCE dechlorination by ZVI and SiH$^{\delta-}$-ZVI in real groundwater collected from an industrial site in Taizhou. **a.** Dechlorination kinetics, **b.** distribution of dechlorination products. All measurements were performed in triplicate (n=3 independent experiments). Data are presented as the mean ± standard deviation. Reaction conditions: [Fe] = 10 g·L^{-1}, [TCE] = 100 μM, 50 mM HEPES buffer, pH 7.0, anoxic conditions, T = 25 °C.

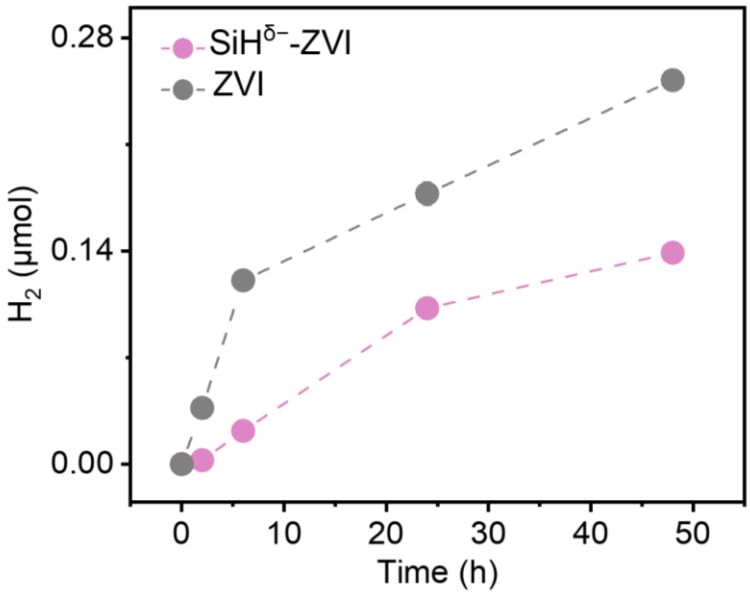

Supplementary Figure 35. Hydrogen evolution in TCE degradation by ZVI and SiH$^{\delta-}$-ZVI in real groundwater collected from an industrial site in Taizhou. All measurements were performed in triplicate (n=3 independent experiments). Data are presented as the mean ± standard deviation. Reaction conditions: [Fe] = 10 g·L^{-1}, [TCE] = 100 μM, 50 mM HEPES buffer, pH 7.0, anoxic conditions, T = 25 °C.

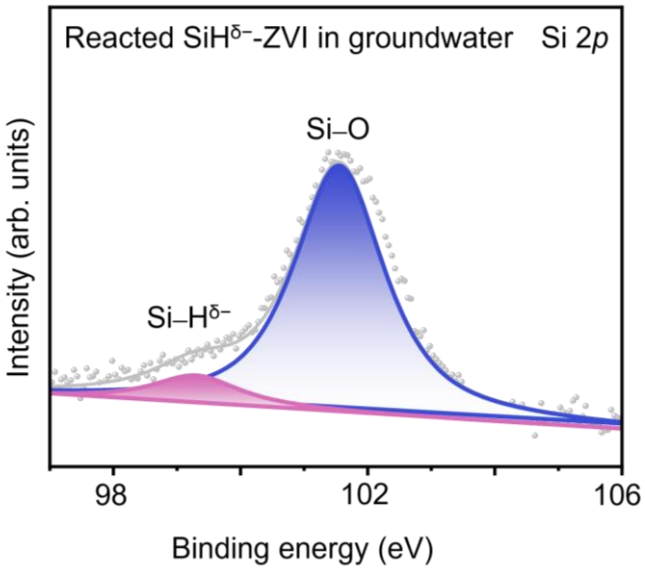

559

560 **Supplementary Figure 36.** Si 2*p* XPS spectra of reacted SiH$^{\delta-}$-ZVI in real groundwater.

Figure 37. Photograph of the continuous-flow column experimental setup for TCE removal from real groundwater collected from an industrial site in Taizhou using $SiH^{\delta-}$-ZVI.

Supplementary Tables

Supplementary Table 1. Summary of the pseudo-first-order rate constants (d^{-1}) for the degradation reaction of FF by $SiH^{\delta-}$-ZVI, Si-ZVI, and ZVI at various stages. Reaction conditions: Fe^0 = 10 $g \cdot L^{-1}$, FF = 20 ppm, 50 mM HEPES, pH 7, anoxic, T = 25 ℃.

Material	Pseudo-first-order rate constants (d^{-1})		
	k_1 (FF→dFF)	k_2 (dFF→ddFF)	k_3 (ddFF→ddFF-F)
$SiH^{\delta-}$-ZVI	66.20 ± 2.82	0.62 ± 0.04	0.028 ± 0.02
Si-ZVI	19.13 ± 3.93	0.083 ± 0.01	/
ZVI	13.81 ± 4.72	0.065 ± 0.01	/

570 **Supplementary Table 2.** Specific surface areas (SA) and surface area-normalized rate
571 constants (k_{SA}) of $SiH^{\delta-}$-ZVI, Si-ZVI, and ZVI for FF degradation. Reaction conditions:
572 Fe^0 = 10 g·L^{-1}, FF = 20 ppm, 50 mM HEPES, pH 7, anoxic, T = 25 °C.

Material	SA ($m^2 \cdot g^{-1}$)	k_{SA} ($L \cdot d^{-1} \cdot m^{-2}$)		
		$k_{1,SA}$ (FF→dFF)	$k_{2,SA}$ (dFF→ddFF)	$k_{3,SA}$ (ddFF→ddFF-F)
$SiH^{\delta-}$-ZVI	1.14	5.80 ± 2.82	0.05 ± 0.04	0.002 ± 0.02
Si-ZVI	0.56	3.41± 3.93	0.01 ± 0.01	/
ZVI	0.40	3.45 ± 4.72	0.01 ± 0.01	/

573

Supplementary Table 3. Kinetic isotope effect (KIE) values calculated from the degradation kinetics of FF by $SiH^{\delta-}$-ZVI and $SiD^{\delta-}$-ZVI. Reaction conditions: Fe^0 = 10 $g \cdot L^{-1}$, FF = 20 ppm, 50 mM HEPES, pH 7, anoxic, T = 25°C.

Material	Pseudo-first-order rate constants (d^{-1})		
	k_1 (FF→dFF)	k_2 (dFF→ddFF)	k_3 (ddFF→ddFF-F)
$SiH^{\delta-}$-ZVI	59.21 ± 6.82	0.64 ± 0.05	0.026 ± 0.01
$SiD^{\delta-}$-ZVI	35.26 ± 3.93	0.37 ± 0.03	0.015 ± 0.02
KIE values	1.67	1.67	1.73

578 **Supplementary Table 4.** Inhibition rate of BIM^+ on the kinetics (d^{-1}) of FF degradation
579 by $SiH^{\delta-}$-ZVI and Si-ZVI. Reaction conditions: Fe^0 = 10 $g \cdot L^{-1}$, FF = 20 ppm, 50 mM
580 HEPES, pH 7, anoxic, T = 25 ℃.

Material	Without BIM^+	With BIM^+	Inhibition rate (%)
	k_1 (FF→dFF)	k_1 (FF→dFF)	
$SiH^{\delta-}$-ZVI	70.92 ± 8.39	13.02 ± 1.05	81.7%
Si-ZVI	16.99 ± 2.45	15.97 ± 2.19	6.1%

581

582 **Supplementary Table 5.** Relative contents of Si–$H^{\delta-}$ and Si-O species in the Si 2*p* XPS
583 spectra of fresh $SiH^{\delta-}$-ZVI and that after 1 h reaction with FF.

Materials	Si–$H^{\delta-}$ (99.2 eV)	Si–O (101.4 eV)
$SiH^{\delta-}$-ZVI	16.3	83.7
Reacted $SiH^{\delta-}$-ZVI	15.3	84.7

584

585 **Supplementary Table 6.** Degradation kinetics and fold enhancement of chlorinated
586 hydrocarbons by $SiH^{\delta-}$-ZVI relative to ZVI (see **Supplementary Figure 33** for kinetic
587 profiles).

Chlorinated hydrocarbons	$k_{obs,TCE}$ (d^{-1})		k_{SA} ($L \cdot d^{-1} \cdot m^{-2}$)		Enhancement ratio ($R_{k_{obs}}$)
	$SiH^{\delta-}$-ZVI	ZVI	$SiH^{\delta-}$-ZVI	ZVI	
TCE	2.52	0.07	0.22	0.02	36.00
PCE	0.92	0.04	0.08	0.01	23.00
CF	1.20	0.25	0.11	0.0625	4.80
cis-DCE	16.90	0.28	1.48	0.07	60.35
trans-DCE	21.67	0.39	1.90	0.10	55.56
VC	6.06	0.41	0.53	0.10	14.78

588

589 **Supplementary Table 7.** Comparative degradation rates of chlorinated hydrocarbons
590 by $SiH^{\delta-}$-ZVI and S-ZVI.

Chlorinated hydrocarbons	$SiH^{\delta-}$-ZVI		S-ZVI		Data Source
	k_M ($h^{-1}\cdot g^{-1}\cdot L$)	k_{SA} ($L\cdot h^{-1}\cdot m^{-2}$)	k_M ($h^{-1}\cdot g^{-1}\cdot L$)	k_{SA} ($L\cdot h^{-1}\cdot m^{-2}$)	
PCE	0.003	0.002	0.001	0.0009	Wu[40]/Gu[23]
TCE	0.01	0.0087	0.021	0.014	
trans-DCE	0.09	0.078	0.004	0.003	
cis-DCE	0.07	0.061	0.0005	0.0004	
VC	0.025	0.021	0.0004	0.0004	

591

Supplementary Table 8. Theoretical electron consumption for the conversion of 1 mol of TCE to various products via reductive dechlorination.

Reactant	Product	Number of required electrons
TCE	Methane	5
	Ethylene	6
	Acetylene	4
	Ethane	8
	Propene	6
	Propane	7.3
	Butene	6
	Butane	7
	Pentene	6
	Pentane	6.8
	Hexene	6
	Hexane	6.7

Supplementary Table 9. Electron efficiency (ε_e) TCE degradation by $SiH^{\delta-}$-ZVI, Si-ZVI, and ZVI after 24 h of reaction (see **Supplementary Figure 33** for experimental data).

Material	ε_e (%)
$SiH^{\delta-}$-ZVI	4.03
Si-ZVI	0.72
ZVI	0.59

599 **Supplementary Table 10.** Compositional and physicochemical parameters of real
600 groundwater collected from an industrial site in Taizhou.

Parameters	Concentration ($\mu g \cdot L^{-1}$)
Ca^{2+}	58440
Mg^{2+}	143670
Na^{+}	777435
TOC	567400
CO_3^{2-}	681000
TCE	115
Hg	7.03
Pb	50.67
Cr(VI)	150
As	98

601

602 **Supplementary Table 11.** Effluent concentrations of TCE, arsenic (As) and hexavalent
603 chromium (Cr (VI)) during the column experiment for TCE removal in real
604 contaminated groundwater collected from an industrial site in Taizhou using $SiH^{\delta-}$-ZVI.

Parameter / Time (d)	TCE ($\mu g \cdot L^{-1}$)	As ($\mu g \cdot L^{-1}$)	Cr ($\mu g \cdot L^{-1}$)
1	0	1.74	1.24
2	0	1.85	3.43
3	0	2.21	2.81
4	0	2.17	3.76
5	0	1.96	3.14
6	0	2.05	2.14
7	0	1.77	1.75
8	0.01	2.13	3.87
9	0.02	2.31	4.24
10	0.02	2.44	3.59

605

606 **Supplementary Table 12.** The manufacturing cost of $SiH^{\delta-}$-ZVI and other ZVI (per
607 ton).

Material	Feed stock ($/ton)			Manufacturing expenses ($/ton)	Other cost ($/ton)[a]	Total cost ($/ton)
$SiH^{\delta-}$-ZVI	mZVI	Na_2SiO_3	H_2O	1000	500	1899.2
	386.67	10.7	1.83			
S-nZVI[22]	$FeCl_3$	$NaBH_4$	$Na_2S_2O_4$	84.09	/	17412.51
	417.2	16688.7	222.52			
TG^{me}-mZVI[8]	mZVI		TG	1000	500	1907.31
	386.67		20.64			
Strained-mZVI[41]	mZVI		B_2O_3	1000	500	1956.67
	386.67		70			

608 a: Other costs include transportation and storage costs.

609 **Supplementary Table 13.** The price of commercial nZVI (per ton).[41]

nZVI	Product name	Manufacturer	Total cost ($/ton)
nZVI	Reactive nanoscale iron particles	Toda Kogyo Corp., Japan	80000
nZVI	NANO FER	NANO IRON s.r.o., Czech Republic	140000
nZVI	Nanoscale iron	Macklin Biochemical Co., Ltd, China	1500000

610

Supplementary References

1 Gong, L. *et al.* Degradation of chloroform by zerovalent iron: Effects of mechanochemical sulfidation and nitridation on the kinetics and mechanism. *Environ. Sci. Technol.* **57**, 9811-9821 (2023). https://doi.org/10.1021/acs.est.3c02039

2 Gong, L., Qiu, X., Tratnyek, P. G., Liu, C. & He, F. FeNx(C)-coated microscale zero-valent iron for fast and stable trichloroethylene dechlorination in both acidic and basic pH conditions. *Environ. Sci. Technol.* **55**, 5393-5402 (2021). https://doi.org/10.1021/acs.est.0c08176

3 Gong, L. *et al.* Coincorporation of N and S into zero-valent iron to enhance TCE dechlorination: Kinetics, electron efficiency, and dechlorination capacity. *Environ. Sci. Technol.* **55**, 16088-16098 (2021). https://doi.org/10.1021/acs.est.1c03784

4 Pan, K., Zhao, Z., Tratnyek, P. G. & Gong, L. Interfacial hydrophobicity-induced desolvation effects on reductive dehalogenation by zero-valent iron. *Water Res.* **293**, 125479 (2026). https://doi.org/10.1016/j.watres.2026.125479

5 Gong, L. *et al.* Mechanochemical molten-salt-assisted surface nitridation promotes electron transfer dechlorination of zerovalent iron. *Environ. Sci. Technol.* **59**, 9802-9811 (2025). https://doi.org/10.1021/acs.est.5c01679

6 Liu, Y., Majetich, S. A., Tilton, R. D., Sholl, D. S. & Lowry, G. V. TCE dechlorination rates, pathways, and efficiency of nanoscale iron particles with different properties. *Environ. Sci. Technol.* **39**, 1338-1345 (2005). https://doi.org/10.1021/es049195r

7 Gong, L. *et al.* Electron-localized active sites enable sustainable 1,2-DCA dechlorination to ethylene by zero-valent iron. *Environ. Sci. Technol.* **60**, 8811-8822 (2026). https://doi.org/10.1021/acs.est.5c15884

8 Zu, J. *et al.* Mechanochemical thioglycolate modification of microscale zero-valent iron for superior heavy metal removal. *Angew. Chem. Int. Ed.* **64**, e202415051 (2025). https://doi.org/10.1002/anie.202415051

9 Hudson, J. M. & Tratnyek, P. G. Electrochemical characterization of pyrogenic carbons: Implications for degradation of groundwater contaminants with carbon-based amendments. *Environ. Sci. Technol.* **59**, 8283-8293 (2025). https://doi.org/10.1021/acs.est.5c00254

10 Xu, J. *et al.* Sulfur loading and speciation control the hydrophobicity, electron transfer, reactivity, and selectivity of sulfidized nanoscale zerovalent iron. *Adv. Mater.* **32**, 1906910 (2020). https://doi.org/10.1002/adma.201906910

11 Chen, Z., Chen, J., Tan, S., Yang, Z. & Zhang, Y. Dechlorination helps defluorination: Insights into the defluorination mechanism of florfenicol by S-nZVI and DFT calculations on the reaction pathways. *Environ. Sci. Technol.* **58**, 2542-2553 (2024). https://doi.org/10.1021/acs.est.3c07435

12 Nonose, N., Cheong, C., Ishizawa, Y., Miura, T. & Hioki, A. Precise determination of dissolved silica in seawater by ion-exclusion chromatography isotope dilution inductively coupled plasma mass spectrometry. *Anal. Chim. Acta* **840**, 10-19 (2014). https://doi.org/10.1016/j.aca.2014.06.018

13 Hu, X., Zhong, M., Wang, F. & Sun, Y. Janus palladium membrane electrode enables competent hydrodehalogenation via hydride transfer. *J.Am.Chem.Soc.* **147**, 28015-28023 (2025). https://doi.org/10.1021/jacs.5c07689
14 Chen, L. *et al.* Accurate identification of radicals by in-situ electron paramagnetic resonance in ultraviolet-based homogenous advanced oxidation processes. *Water Res.* **221**, 118747 (2022). https://doi.org/10.1016/j.watres.2022.118747
15 Li, M. *et al.* Surface FeIV═O induced highly selective phenol polymerization via proton-coupled electron transfer. *J.Am.Chem.Soc.* **147**, 31165-31174 (2025). https://doi.org/10.1021/jacs.5c09972
16 Ze, H. *et al.* In Situ probing the structure change and interaction of interfacial water and hydroxyl intermediates on $Ni(OH)_2$ surface over water splitting. *J.Am.Chem.Soc.* **146**, 12538-12546 (2024). https://doi.org/10.1021/jacs.4c00948
17 Wang, Y.-H. *et al.* In situ raman spectroscopy reveals the structure and dissociation of interfacial water. *Nature* **600**, 81-85 (2021). https://doi.org/10.1038/s41586-021-04068-z
18 Liao, M. *et al.* Silicate-confined hydrogen on nanoscale zerovalent iron for efficient defluorination reactions. *J.Am.Chem.Soc.* **147**, 3402-3411 (2025). https://doi.org/10.1021/jacs.4c14261
19 Jiang, G. *et al.* Identification of active hydrogen species on palladium nanoparticles for an enhanced electrocatalytic hydrodechlorination of 2,4-dichlorophenol in water. *Environ. Sci. Technol.* **51**, 7599-7605 (2017). https://doi.org/10.1021/acs.est.7b01128
20 Mu, Z. *et al.* Critical role of hydrogen sorption kinetics in electrocatalytic CO_2 reduction revealed by on-chip in situ transport investigations. *Nat. Commun.* **13**, 6911 (2022). https://doi.org/10.1038/s41467-022-34685-9
21 He, F., Gong, L., Fan, D., Tratnyek, P. G. & Lowry, G. V. Quantifying the efficiency and selectivity of organohalide dechlorination by zerovalent iron. *Environ. Sci.: Processes Impacts* **22**, 528-542 (2020). https://doi.org/10.1039/C9EM00592G
22 Chen, C. *et al.* Lattice-sulfur-impregnated zero-valent iron crystals for long-term metal encapsulation. *Nature Sustainability* **7**, 1264-1272 (2024). https://doi.org/10.1038/s41893-024-01409-4
23 Gu, Y., Wang, B., He, F., Bradley, M. J. & Tratnyek, P. G. Mechanochemically sulfidated microscale zero valent iron: Pathways, kinetics, mechanism, and efficiency of trichloroethylene dechlorination. *Environ. Sci. Technol.* **51**, 12653-12662 (2017). https://doi.org/10.1021/acs.est.7b03604
24 Hu, X. *et al.* Lattice engineered nanoscale Fe^0 for selective reductions. *Nat. Water* **2**, 84-92 (2024). https://doi.org/10.1038/s44221-023-00175-5
25 Zhou, Q. *et al.* Sulfur-impregnated nanoscale Fe(0) via ball milling and desulfurization of commercial microscale pyrite for groundwater remediation. *Environ. Sci. Technol.* **59**, 26207-26216 (2025). https://doi.org/10.1021/acs.est.5c03118
26 (ITRC), I. T. R. C. Permeable reactive barrier: Technology update. Report No. PRB-5, (Interstate technology & regulatory council, PRB: technology update team, Washington, D.C., 2011).

27 Johnson, R. & Tratnyek, P. Remediation of explosives in groundwater using a zero-valent iron permeable reactive barrier. Report No. ESTCP Project ER-0223, (Environmental Security Technology Certification Program (ESTCP), Arlington, VA, 2008).
28 Qin, M. *et al.* Surfactant-enhanced $Cu^{\delta+}$ and induced electrostatic forces promote the electrocatalytic deuteron-dechlorination of trichloroacetic acid. *Nat. Commun.* **16**, 10365 (2025). https://doi.org/10.1038/s41467-025-65333-7
29 Kresse, G. & Furthmüller, J. Efficiency of ab-initio total energy calculations for metals and semiconductors using a plane-wave basis set. *Computational Materials Science* **6**, 15-50 (1996). https://doi.org/10.1016/0927-0256(96)00008-0
30 Kresse, G. & Furthmüller, J. Efficient iterative schemes for ab initio total-energy calculations using a plane-wave basis set. *Phys. Rev. B.* **54**, 11169-11186 (1996). https://doi.org/10.1103/PhysRevB.54.11169
31 Perdew, J. P., Burke, K. & Ernzerhof, M. Generalized gradient approximation made simple. *Phys. Rev. Lett.* **77**, 3865-3868 (1996). https://doi.org/10.1103/PhysRevLett.77.3865
32 Blöchl, P. E. Projector augmented-wave method. *Phys. Rev. B.* **50**, 17953-17979 (1994). https://doi.org/10.1103/PhysRevB.50.17953
33 Kresse, G. & Joubert, D. From ultrasoft pseudopotentials to the projector augmented-wave method. *Phys. Rev. B.* **59**, 1758-1775 (1999). https://doi.org/10.1103/PhysRevB.59.1758
34 Fu, Q. *et al.* Interface-confined ferrous centers for catalytic oxidation. **328**, 1141-1144 (2010). https://doi.org/10.1126/science.1188267
35 Li, M. *et al.* Phosphate modification enables high efficiency and electron selectivity of nZVI toward Cr(VI) removal. *Appl. Catal. B Environ* **263**, 118364 (2020). https://doi.org/10.1016/j.apcatb.2019.118364
36 Li, X. Q. & Zhang, W. X. Iron nanoparticles: The core-shell structure and unique properties for Ni(II) sequestration. *Langmuir* **22**, 4638-4642 (2006). https://doi.org/10.1021/la060057k
37 Ling, L., Huang, X., Li, M. & Zhang, W.-x. Mapping the reactions in a single zero-valent iron nanoparticle. *Environ. Sci. Technol.* **51**, 14293-14300 (2017). https://doi.org/10.1021/acs.est.7b02233
38 Mu, Y., Jia, F., Ai, Z. & Zhang, L. Iron oxide shell mediated environmental remediation properties of nano zero-valent iron. *Environmental Science: Nano* **4**, 27-45 (2017). https://doi.org/10.1039/C6EN00398B
39 Niu, K., Chen, L., Rosen, J. & Björk, J. CO_2 hydrogenation with high selectivity by single Bi atoms on mxenes enabled by a concerted mechanism. *ACS Catal.* **14**, 1824-1833 (2024). https://doi.org/10.1021/acscatal.3c04480
40 Wu, S. *et al.* Reductive dechlorination of chlorinated ethenes by ball milled and mechanochemically sulfidated microscale zero valent iron: A comparative study. *J. Hazard. Mater.* **446**, 130730 (2023). https://doi.org/10.1016/j.jhazmat.2023.130730
41 Wei, K. *et al.* Strained zero-valent iron for highly efficient heavy metal removal. *Adv. Funct. Mater.* **32**, 2200498 (2022). https://doi.org/ 10.1002/adfm.202200498